JGR Solid Earth

RESEARCH ARTICLE
10.1029/2021JB023241

# A Seismic Tomography, Gravity, and Flexure Study of the Crust and Upper Mantle Structure of the Emperor Seamounts at Jimmu Guyot

**C. Xu[1,2], R. A. Dunn[2], A. B. Watts[3], D. J. Shillington[4], I. Grevemeyer[5], L. Gómez de la Peña[5], and B. B. Boston[6]**

[1]Key Lab of Submarine Geosciences and Prospecting Techniques, Ministry of Education, and College of Marine Geosciences, Ocean University of China, Qingdao, China, [2]Department of Earth Sciences, School of Ocean and Earth Science and Technology, University of Hawaii at Manoa, Honolulu, HI, USA, [3]Department of Earth Sciences, University of Oxford, Oxford, UK, [4]School of Earth and Sustainability, Northern Arizona University, Flagstaff, AZ, USA, [5]GEOMAR Helmholtz Centre for Ocean Research, Kiel, Germany, [6]Lamont Doherty Earth Observatory of Columbia University, Palisades, NY, USA

**Abstract** The intraplate Hawaiian-Emperor Seamount Chain has long been considered a hotspot track generated by the motion of the Pacific plate over a deep mantle plume, and an ideal feature therefore for studies of volcanic structure, magma supply, plume-crust interaction, flexural loading, and upper mantle rheology. Despite their importance as a major component of the chain, the Emperor Seamounts have been relatively little studied. In this paper, we present the results of an active-source wide-angle reflection and refraction experiment conducted along an ocean-bottom-seismograph (OBS) line oriented perpendicular to the seamount chain, crossing Jimmu guyot. The tomographic *P* wave velocity model, using ~20,000 travel times from 26 OBSs, suggests that there is a high-velocity (>6.0 km/s) intrusive core within the edifice, and the extrusive-to-intrusive ratio is estimated to be ~2.5, indicating that Jimmu was built mainly by extrusive processes. The total volume for magmatic material above the top of the oceanic crust is ~$5.3 \times 10^4$ km$^3$, and the related volume flux is ~0.96 m$^3$/s during the formation of Jimmu. Under volcanic loading, the ~5.3-km-thick oceanic crust is depressed by ~3.8 km over a broad region. Using the standard relationships between V*p* and density, the velocity model is verified by gravity modeling, and plate flexure modeling indicates an effective elastic thickness ($T_e$) of ~14 km. Finally, we find no evidence for large-scale magmatic underplating beneath the pre-existing crust.

**Plain Language Summary** As lithospheric plates move across mantle hotspots, melts will rise and pass through the plate to form a series of volcanos. The Hawaiian-Emperor Seamount Chain is one of the Earth's most well-known hotspot tracks and an ideal laboratory therefore for studying the nature and characteristics of volcano building and the extent to which oceanic plates bend under the weight of these volcanos, which is an indication of oceanic plate strength. As a major component of the chain, the Emperor Seamounts have been relatively little studied. To address these issues, we carried out an active-source seismic imaging experiment across the Emperor Seamounts at Jimmu guyot. The seismic velocity image reveals that Jimmu has a core made from magmas that froze within its edifice but was built mainly by volcanic processes. Due to volcanic loading, the oceanic crust is depressed by ~3.8 km. The density structure derived from the tomographic image well-predicts observed gravity, while plate flexure modeling indicates an effective elastic thickness of ~14 km, suggesting that the oceanic plate on which the Emperor chain was built was weaker at the time of volcano formation than the Hawaiian Ridge.

**Key Points:**

- Seismic tomography experiment reveals crust and upper mantle structure along a 495-km-long east-west line crossing the Emperor Seamounts
- Jimmu guyot was built mainly by extrusive processes, and the underlying ~5.3-km-thick oceanic crust was depressed by ~3.8 km
- There is no evidence for large-scale magmatic underplating beneath the edifice

**Supporting Information:**

Supporting Information may be found in the online version of this article.

**Correspondence to:**

C. Xu,
xuchong5751@stu.ouc.edu.cn

**Citation:**

Xu, C., Dunn, R. A., Watts, A. B., Shillington, D. J., Grevemeyer, I., Gómez de la Peña, L., & Boston, B. B. (2022). A seismic tomography, gravity, and flexure study of the crust and upper mantle structure of the Emperor Seamounts at Jimmu guyot. *Journal of Geophysical Research: Solid Earth*, *127*, e2021JB023241. https://doi.org/10.1029/2021JB023241

Received 15 SEP 2021
Accepted 19 MAY 2022

**Author Contributions:**

**Conceptualization:** C. Xu, R. A. Dunn, A. B. Watts, D. J. Shillington
**Data curation:** C. Xu, A. B. Watts, I. Grevemeyer
**Formal analysis:** C. Xu
**Funding acquisition:** R. A. Dunn
**Investigation:** C. Xu, R. A. Dunn, A. B. Watts, D. J. Shillington, L. Gómez de la Peña, B. B. Boston
**Methodology:** R. A. Dunn
**Project Administration:** R. A. Dunn
**Resources:** R. A. Dunn, D. J. Shillington
**Software:** R. A. Dunn
**Supervision:** R. A. Dunn
**Validation:** R. A. Dunn
**Visualization:** C. Xu, A. B. Watts
**Writing – original draft:** C. Xu



## 1. Introduction

The Hawaiian-Emperor Seamounts, an intraplate volcanic chain located in the northwest Pacific Ocean, has long been considered a hotspot track generated by the motion of the Pacific plate over a deep mantle plume (Morgan, 1971; Wilson, 1963). As individual volcanos of the chain grow, they apply a downward load on the underlying seafloor and progressively deform the lithosphere beneath the load and up on its flanks. The resulting flexure is manifest in the deep bathymetric depression, or "moat," that flanks part of the volcanic chain, the crustal structure in the vicinity of the edifice (Grevemeyer et al., 2001b; McNutt, 1984; Rees et al., 1993; Watts & ten Brink, 1989) and the uplift and subsidence history of pre-existing volcanoes. Studies of lithospheric flexure due

**Writing – review & editing:** R. A. Dunn, A. B. Watts, D. J. Shillington, I. Grevemeyer, L. Gómez de la Peña, B. B. Boston

to volcano loading along the seamount chain have been significant for the investigation of the stress state, rigidity, and rheological properties of the oceanic lithosphere (Calmant, 1987; Watts, 1978; Watts & Cochran, 1974; Watts & Ribe, 1984). Important considerations that control the amount of flexure include the size and distribution of the load, the physical properties of the material that infills flexure, and the thermal age of oceanic lithosphere at the time of loading (Parsons & Sclater, 1977; Watts, 1978; Zhong & Watts, 2013).

A poorly understood aspect of hotspot chain volcanism, one that impacts investigation of plate loading and rheological models, is the vertical and horizontal distributions of material added to the crust by magmatic activity. Previous studies have suggested a range of possibilities from volcanic construction being completely confined to the region above the pre-existing oceanic crust (e.g., Pim et al., 2008), to some new material added within the oceanic crust (e.g., Caress et al., 1995; Contreras-Reyes et al., 2010), to some material "underplated" to the bottom of the old oceanic crust (e.g., Grevemeyer et al., 2001a; ten Brink & Brocher, 1987; Watts et al., 1985). Moreover, the ratio between the volume of extrusive and intrusive volcanism is an important constraint on the processes of volcano growth and the origin of intraplate volcanism.

Seismic refraction studies using ocean-bottom seismographs (OBSs) and ship-based airgun shots have revealed high *P* wave intracrustal regions, suggestive of magmatic intrusive bodies beneath some seamounts. Caress et al. (1995) reported an unusually high-velocity (7.3–7.75 km/s) lower-crustal region beneath the Marquesas Islands although the velocity was not directly constrained in the deepest crust. Contreras-Reyes et al. (2010) revealed a high-velocity (7.2–7.6 km/s) intracrustal region beneath a seamount in the Louisville Ridge, and suggested that ultramafic rocks had been intruded as sills into the crust, rather than underplated beneath the oceanic crust.

The evidence for magmatic underplating beneath the flexed oceanic crust varies strongly in ocean basins, and the underlying mechanism controlling differences are still poorly understood. Watts et al. (1985) and ten Brink and Brocher (1987) collected both multichannel seismic reflection data and expanding spread profile (ESP) refraction data cross the Hawaiian Ridge near Oahu. They found a ∼4-km-thick, ∼300-km-wide, high-velocity (7.4–7.9 km/s) body with a reflective base beneath the oceanic crust, and interpreted it as a deep crustal sill complex that underplates the pre-existing oceanic crust beneath the ridge (ten Brink & Brocher, 1987; Watts & ten Brink, 1989; Watts et al., 1985). Thereafter, magmatic underplating was suggested at several seamounts, e.g., the Marquesas hotspot chain (Caress et al., 1995; McNutt & Bonneville, 2000; Wolfe et al., 1994), the La Reunion Island (Charvis et al., 1999; Gallart et al., 1999), the Great Meteor Seamount (Weigel & Grevemeyer, 1999), and the Ninetyeast Ridge (Grevemeyer & Flueh, 2000; Grevemeyer et al., 2001a). However, some seamounts, such as the Canary Islands (Canales et al., 2000; Watts et al., 1997), the Society Island hotspot chain (Grevemeyer et al., 2001b), the Musicians Seamounts (Kopp et al., 2003), the Cape Verde Islands (Pim et al., 2008), the Louisville Ridge (Contreras-Reyes et al., 2010), and the Cocos (Walther, 2003), Carnegie (Sallarès et al., 2003), and Malpelo (Sallarès et al., 2005) Ridges of the Galapagos Volcanic Province, do not show evidence of magmatic underplating. Moreover, the existence of magmatic underplating was also questioned by Lindwall (1988) on the basis of a single ESP on the Hawaiian Ridge between Oahu and Molokai.

One possible reason for variations in the style of magmatic emplacement beneath seamounts and hotspot chains worldwide is the age of the oceanic lithosphere at the time of volcanic loading, with intrusion being favored for seamounts built on young lithosphere and magmatic underplating favored for seamounts built on old lithosphere (Contreras-Reyes et al., 2010).

The Emperor Seamounts comprise an age-progressive seamount chain that extends across the Northwest Pacific Ocean from the Hawaiian-Emperor bend (∼47–50 Ma) to Detroit (81-75 Ma) and Meiji (>82 Ma) seamounts in the northwest Pacific (Clague & Dalrymple, 1987; Duncan & Keller, 2004). The underlying oceanic lithosphere formed during the Cretaceous Normal Superchron (CNS; Seton et al., 2020). The volcanic production rate of the Emperor Seamount Chain, as estimated from the bathymetry and its isostatic compensation, displays a significantly lower value than the Hawaiian Ridge (Van Ark & Lin, 2004; Vidal & Bonneville, 2004; Wessel, 2016; White, 1993). Seismic investigations of loading of the plate along the Emperor Seamounts, and the resulting flexure, have the potential to constrain volcanic production rates, as well as the rheological properties of oceanic lithosphere that was significantly younger and nearer to the crest of a mid-ocean ridge during loading than at the Hawaiian Islands.

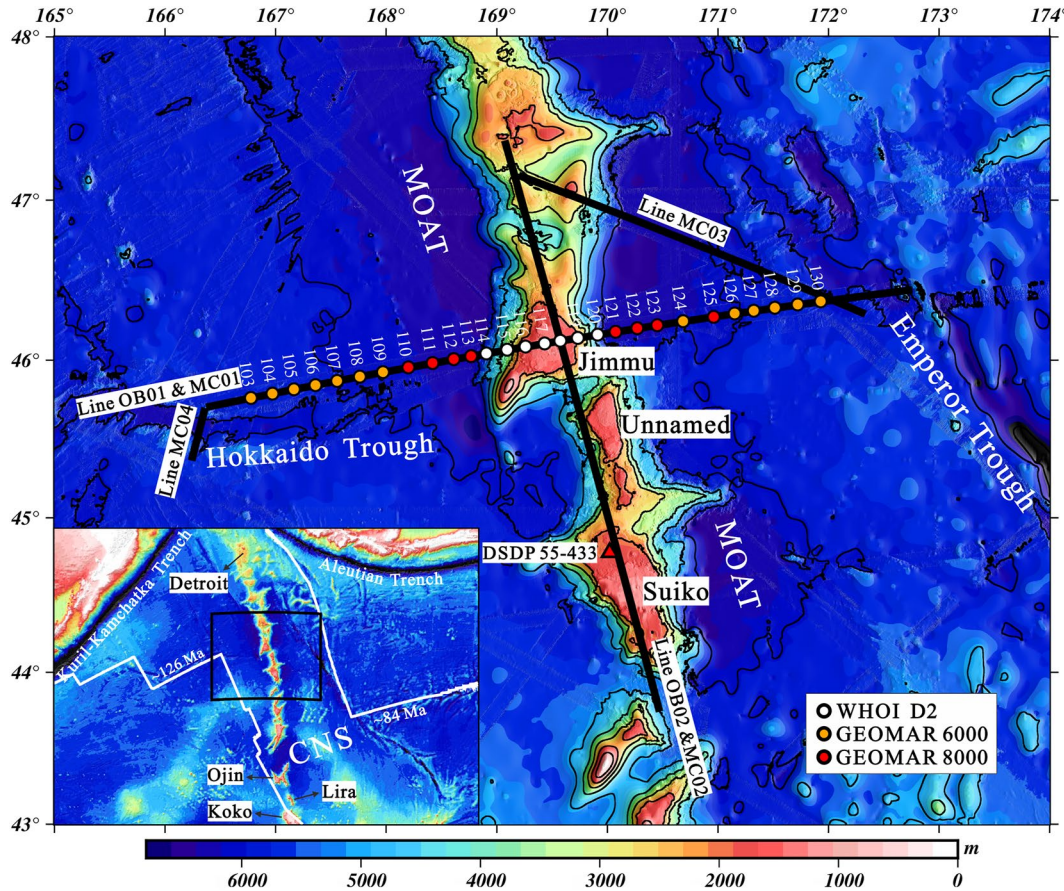


**Figure 1.** (Inset) The location of the study area in the Northwest Pacific Ocean and details of the seismic experiment reported here. The white solid lines indicate the boundary of the Cretaceous Normal Superchron (CNS; Seton et al., 2020). The black box indicates the area shown in the main figure. (Main figure) Layout of the seismic experiment overlain on a map of bathymetry. White, orange, and red circles indicate the locations of the different types of ocean-bottom seismographs used in this study; black lines indicate airgun shot lines. Only Line OB01 (OBS 103–130) is analyzed in this paper. The location of Deep Sea Drilling Project (DSDP) site 55-433 is indicated by the red filled triangle (Jackson et al., 1980). Bathymetry is derived from a compilation of data from cruise MGL1902 (Watts et al., 2020) combined with a global grid derived from satellite and existing multibeam bathymetry data (Tozer et al., 2019). Both Figures 1 and 2 were constructed using GMT 6 (Wessel et al., 2019).

To investigate the volcanic edifice structure, and the underlying oceanic crust and upper mantle structure, beneath the Emperor Seamounts, we carried out an active-source wide-angle refraction experiment in April-June 2019 (Figure 1). The experiment included two OBS seismic lines for tomographic imaging, one oriented along the crest of the seamounts (Line OB02), the main results of which are presented in Watts et al. (2021), and the other perpendicular to it (Line OB01), with an approximate east-west orientation, which is the focus of this paper. Concurrent with the seismic experiment, we acquired shipboard swath bathymetry and free-air gravity anomaly data and so are able to present a joint seismic, gravity, and lithospheric flexural analysis of the data sets. The results provide new insights into processes of volcano growth and plate loading, magmatic flux in the Emperor Seamount Chain, and the rheological properties of the upper mantle.

## 2. Study Area

### 2.1. Geologic and Tectonic Context

The oceanic crust underlying the study area was formed by seafloor spreading at the Pacific-Farallon Ridge (e.g., Seton et al., 2012; Wright et al., 2016), with a full rate of ~90–110 mm/yr (Müller et al., 2008). Seismic Line

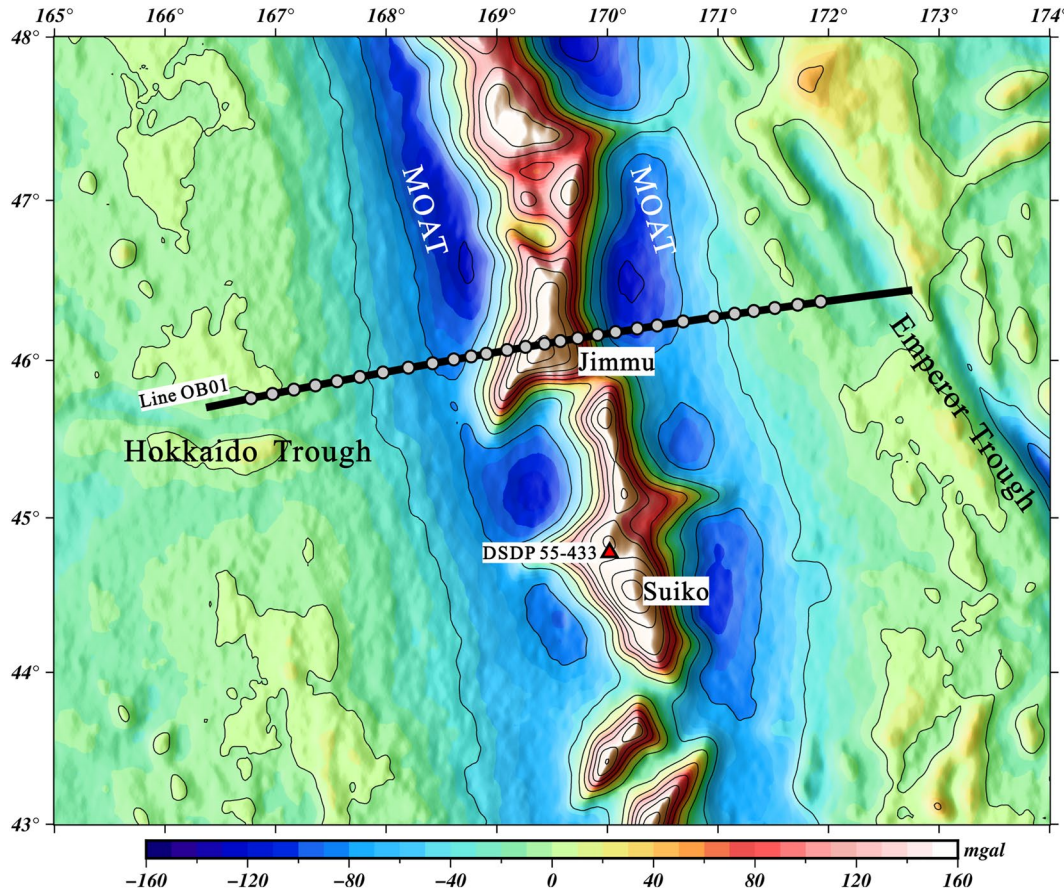


**Figure 2.** Map of the free-air gravity anomaly across the study area showing Line OB01. The contrasting positive and negative gravity anomalies along the Emperor Seamount Chain reflect the loading and flexure of the Pacific oceanic plate (e.g., Watts & Cochran, 1974). The Emperor and, to a lesser extent, the Hokkaido troughs are visible as free-air gravity anomaly lows. The gravity map is based on the global compilation V28.1, derived from satellite altimeter data (Sandwell et al., 2019).

OB01 intersects the Emperor Seamount Chain at Jimmu guyot (Dietz, 1954), where the water depth on the crest of the guyot is ~1,300 m (Figure 1). Elsewhere along the seismic line, water depth varies from ~5,800 m at the ends of the line to ~6,300 m in the moat (Figure 1). Therefore, along the line, the guyot rises ~5,000 m above the depth of the surrounding seafloor.

No direct age information is available for Jimmu. However, Suiko guyot, located ~220 km to the south of Jimmu (Figure 1), has been drilled and sampled by the Deep Sea Drilling Project (DSDP), and $^{40}Ar/^{39}Ar$ surface sample ages from hole DSDP55-433 indicate the guyot formed 60.9 ± 0.3 Ma (Dalrymple et al., 1980; Sharp & Clague, 2006). Using a hotspot-plate relative speed of ~5.7 cm/yr, the distance between Jimmu and Suiko guyots implies an age difference of ~4 Ma (Doubrovine et al., 2012; O'Connor et al., 2013; Sharp & Clague, 2006; Tarduno et al., 2003) and an age of ~65 Ma for Jimmu guyot. By contrast, the age of the lithosphere in the study area is ~120 Ma (Seton et al., 2020). Thus, the age of the oceanic lithosphere at the time of volcanic loading at Jimmu guyot was ~55 Myr, which is significantly younger than the ~90-Myr-old lithosphere currently being loaded at Hawaii. This age difference is reflected in differences in the effective elastic thickness ($T_e$) of the lithosphere, a measure of its flexural rigidity or resistance to deformation, during seamount formation. For example, gravity and geoid data suggest that $T_e$ is 15 ± 2.5 km at the Emperor Seamounts, and 27.2 ± 2.5 km beneath the Hawaiian Ridge (Watts, 1978; Watts & Ribe, 1984; Watts et al., 2013).

Other major geologic features located along Line OB01 are the Emperor and Hokkaido troughs, which are visible in both swath bathymetry and free-air gravity anomaly data (Figures 1 and 2). The ~1,500-km-long northwest

trending Emperor Trough lies along the eastern edge of the study area (Figure 1). It was first recognized by the U.S. Environmental Science Services Administration's (ESSA) Pacific Oceanographic Research Laboratory during research expeditions in 1968 and 1969 (Erickson et al., 1970), and was suggested to be a transform fault formed by the spreading between the Pacific and Izanagi plates during the CNS (Atwater et al., 1993; Gordon, 1982; Hilde et al., 1977; Larson & Chase, 1972; Mammerickx & Sharman, 1988; Seton et al., 2012; Smoot & Lowrie, 1985; Wright et al., 2016), while others have proposed that it was a rift formed during the early stages of Kula plate formation (Woods & Davies, 1982). In general, the bathymetric relief across most transects of the Emperor Trough is ~1,000-2,500 m, but is more modest, ~300 m, where it intersects Line OB01 (Erickson et al., 1970; Farrar & Dixon, 1981).

The Hokkaido Trough is located along the western portion of the seismic line (Figure 1). First charted by Chase et al. (1968), this ~1,000-km-long east-west trending bathymetric feature has a shallower relief than the Emperor Trough (Chase et al., 1968; Green & Fleischer, 1980; Mammerickx & Sharman, 1988) and a subtler expression in the free-air gravity anomaly map (Figure 2). It is thought to be possibly a failed spreading ridge that formed between the Pacific plate and either the Izanagi or Kula plate (Mammerickx & Sharman, 1988; Seton et al., 2012).

### 2.2. Previous Seismic Studies

Despite forming part of the iconic, hotspot generated, Hawaiian-Emperor Seamount Chain, no modern detailed deep seismic imaging has ever been carried out over the Emperor Seamounts. The first two-ship seismic refraction measurement across the Emperor Seamounts was made between Ojin guyot and Lira seamount (inset of Figure 1) during June 1966 as part of the United States and Japan Science Cooperation Program (Den et al., 1969). In their study, the thickness of the crust beneath the Emperor Seamounts was determined to thin from ~10.3 km, at 150 km to the west of the ridge, to ~6.2 km under the ridge axis. In contrast, layer 2A, with a velocity of ~3.7 km/s, thickened toward the seamount chain (Den et al., 1969). In a later study, located ~100 km south of the Den et al. (1969) profile, near the northwestern flank of Koko Seamount (inset of Figure 1), seismic refraction data (acquired with only two OBSs) indicated that the crustal thickness beneath the ridge flank is ~9 km, without any detectable dip to the base of the crust (Furukawa et al., 1980). Earlier sonobuoy data collected to the east and to the south of Koko Seamount showed a similar result to that of Den et al. (1969), such that the thickness of layer 2A tended to increase toward the edifice and has a similar upper crustal velocity-depth structure to that in the Furukawa et al. (1980) study (Houtz, 1976). Using single-channel seismic reflection profile data, Kerr et al. (2005) characterized the seismic stratigraphy of Detroit Seamount (inset of Figure 1) and suggested renewed volcanism ~25 Ma after the end of the main shield-building phase (Kerr et al., 2005).

In 1976, a single-channel seismic reflection experiment was carried out across an unnamed guyot between Jimmu and Suiko guyots (Greene et al., 1978; Figure 1). Although no deep information was obtained, the shallow seismic profile indicated that the flat summit of the elongate seamount is capped by ancient coral reefs. This result is consistent with dredge samples and drill hole data (DSDP55-433) on Suiko guyot (Figure 1), where shallow-water reef fossils were recovered (Dalrymple et al., 1980). Greene et al. (1978) proposed that the unnamed guyot was once within ~10 m of, or probably above, sea level, but eventually sank to its present depth (~1,300–1,400 m) due to plate subsidence or flexure.

## 3. Experiment and Data

### 3.1. Seismic Data

The seismic data for this study were acquired in April-June 2019 during cruise MGL1902 aboard R/V *Marcus G. Langseth*. The experiment included two seismic refraction lines (Lines OB01 and OB02), one oriented along the axis of the Emperor Seamounts in the region of Jimmu and Suiko guyots (Watts et al., 2021) and the other perpendicular to it, crossing Jimmu in an approximate east-west orientation (Figure 1). Multichannel seismic reflection profile data (Lines MC01-04) were also collected (Boston et al., 2019). In this study, we analyze the refraction and wide-angle reflection data from the 495-km-long east-west "dip" profile (Figure 1). Along this line, 28 short-period OBSs from GEOMAR and OBSIC-WHOI were deployed with an average spacing of 16 km. However, stations 123 and 126 did not return data, so 26 instruments were used in this study. Each OBS contained

a hydrophone and a three-component geophone that recorded at a sampling rate of 250 and 200 samples/s for the GEOMAR and OBSIC instruments, respectively. The seismic source was *Langseth's* 4-string, 36-element, 6,600-cubic-inch airgun array, towed at 12-m depth with a nominal shot spacing of ~300 m at a speed of ~4.5 knots.

Data recorded on each OBS were converted to SEG-Y format and time corrected for clock drift. Water wave travel times were used to locate the instruments on the seafloor. For the water wave travel time picking, the data were band-pass filtered with a minimum-phase 5–45 Hz Butterworth filter, and the travel times of the first and second water wave arrivals were picked within a few kilometers range for each instrument. By comparing travel times of the first and second water wave, we determined a consistent timing shift between the reported shot time (via the ship's shot algorithm) and an estimated shot time (via the water wave comparison) of 150 ms, which was added to the time base of each instrument. This timing shift could be due to the difference between the firing time indicated by the shot system and the time it occurred due to a mechanical delay of the airgun and bubble pulse. Instrument locations were then determined from travel times of the direct water wave using a Bayesian grid-search algorithm (Dunn & Hernandez, 2009). The time shift greatly improved the data misfit and instrument positions, in that their final locations are found to be within a few meters of the seafloor, as determined by multibeam bathymetry, rather than being consistently located with a large depth bias.

For solid-earth phase identification and travel time picking, the data were refiltered with a minimum-phase 5–25 Hz Butterworth filter, and a range-dependent amplitude gain was applied to correct for geometric spreading and energy loss. To improve visual phase identification, static corrections for bathymetry were applied to all the record sections. To improve trace-to-trace coherency for some noisy stations, a small amount of trace-to-trace averaging was performed after correcting for trace move-out. All arrivals of *P* waves were manually picked on either the vertical geophone (*Z* channel) or hydrophone (*H* channel) channels, or both, depending on data quality.

A number of different *P* wave phases were identified in the record sections (Figure 3). On an individual instrument, the particular combination of phases and their arrival times depends in large part on the station's distance from the crest of the Emperor Seamount Chain. Away from the seamount chain, typical seismic phases for oceanic crust are observed, but as the seamounts are approached, the crust gets noticeably thicker and additional seismic phases appear in the records. Where appropriate, we used the often-stronger water-wave multiple (e.g., Meléndez et al., 2014) as a guide to picking faint first arrivals, especially for *PmP* and *Pn* phases, so as not to miss the first arriving energy. For all seismic phases, we performed shot-receiver reversal comparisons to check for consistency, as well as careful checks of the data misfit, computed with respect to the tomographic image, to look for any systematic biases.

At the western and eastern ends of the seismic line, on relatively old Pacific oceanic crust, data records exhibit sets of arrivals (Figures 3a and 3f) that include a first-arrival near-station shallowly refracted phase (*P*1), with low apparent velocity (~2–5 km/s) and short shot-receiver offsets (<~6 km). We interpret this phase as largely a refraction in the sediment layer, and it extends to larger source-receiver offsets as the moat is approached and the sediments presumably thicken. With increasing range, a higher-velocity refraction (*P*2) is observed, which we interpret as a refraction in the upper oceanic crust, seismic layer 2 (e.g., Houtz & Ewing, 1976), with apparent velocities of ~5.0–6.5 km/s, which is typical of older oceanic crust (Houtz & Ewing, 1976). Given the large water depth and presence of a sediment layer, forward modeling suggests that lower velocities at the top of layer 2 as seen near mid-ocean ridges (e.g., Dunn et al., 2017), if they exist, would largely be masked by the *P*1 phase. At the intersection of the *P*1 and *P*2 phases, there is often a triplication or reflection-like phase (*P*2*P*), which we interpret as the top of the oceanic crust. Despite the ambiguity, we model it as a reflection, similar to approaches used elsewhere for layer 2A reflections (e.g., Harding et al., 1993) and *PmP* reflections (e.g., Dunn et al., 2005). Therefore, even if not a true reflection, the depth of the sharp transition in V*p* values that gives rise to the change in slope of the first arrivals (between *P*1 and *P*2) is tracked by the *P*2*P* arrival acting as if it followed a reflector. In the moat areas, where the sediment thickness is large, *P*2*P* is more clearly observed (Figures 3g and 3h). But as the sediment thins way from the moat in both directions, *P*2*P* phase identification becomes more subjective and the assigned pick uncertainty was much larger than for the moat areas. In addition, beneath the flanks of the edifice, the *P*2*P* phase becomes much harder to identify, as it tends to overlap other phases such as *PmP*, and at times appears to be more than one arrival (e.g., as if there is more than one reflector). The *P*2*P* arrivals are not clearly observable directly below the edifice. In places, high-amplitude secondary energy does exist, but without a clear onset or a clear change in gradient of the refracted phases, or is confused with a triplication over the

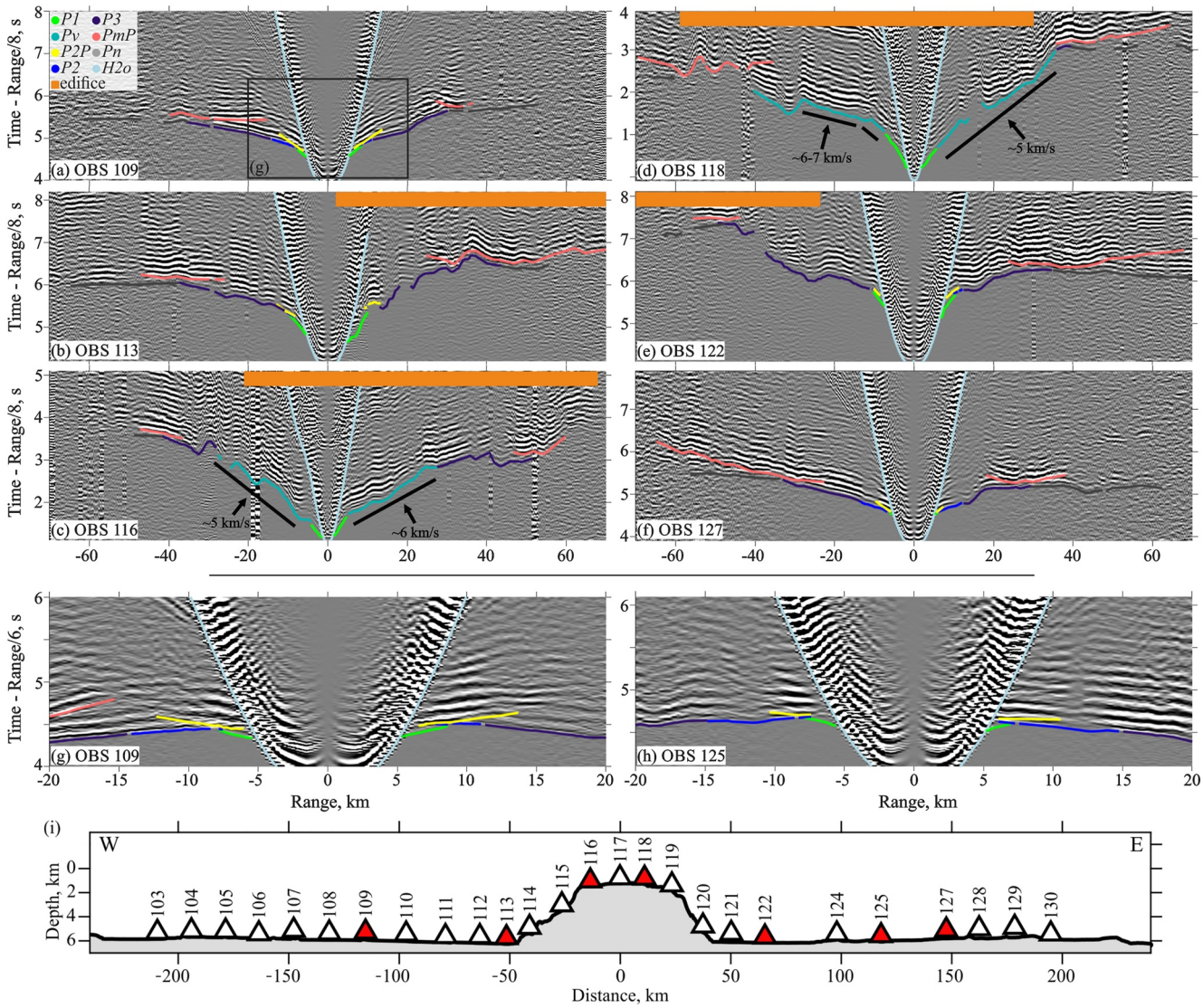


**Figure 3.** Examples of wide-angle seismic record sections with picks of different phases indicated by different colors (see legend in (a) for phase-color code, orange bars indicate the spatial position of the edifice). The seismic data have been band-pass filtered, corrected for seafloor topography and scaled by range. The locations of the stations for each record section are marked by red triangles in the lowermost plot. Lines on (c) and (d) next to the *Pv* phase are to emphasize the sharp increase in V*p* between rays that penetrate the outer region of the edifice to those that penetrate its core. (g) and (h) are "blowups" with an expanded vertical scale. See the Supporting Information for a display of all record sections.

inner core of the edifice (see below), and for other records nothing resembling a *P2P* phase was available. This suggests the lack of a significant velocity or impedance contrast between the base of the intrusive complex that comprises the core of the edifice and the underlying oceanic crust. Nevertheless, for stations and shots in the moat regions, the *P2P* phase exhibits much larger range and travel time changes for the transition depth than the uncertainty of the *P2P* picks (Figure S3a in Supporting Information S1). Therefore, we feel fairly confident that *P2P* can be used across the moat areas to constrain first-order changes in depth of the top of the oceanic crust in a broad sense.

Beyond *P*1 and *P*2, the first-arrival refraction (*P*3) has an apparent phase velocity of ~7 km/s, which we interpret as turning in the lower oceanic crust, seismic layer 3 (e.g., Christeson et al., 2019; Grevemeyer et al., 2018). The transition from *P*2 to *P*3 is not always obvious, but is inconsequential to the imaging below, since the two phases are modeled as single continuous phase. Additionally, wide-angle reflections from the crust-mantle boundary, high-amplitude *PmP* arrivals, and ~8 km/s *Pn* refractions turning in the uppermost mantle are evident in most

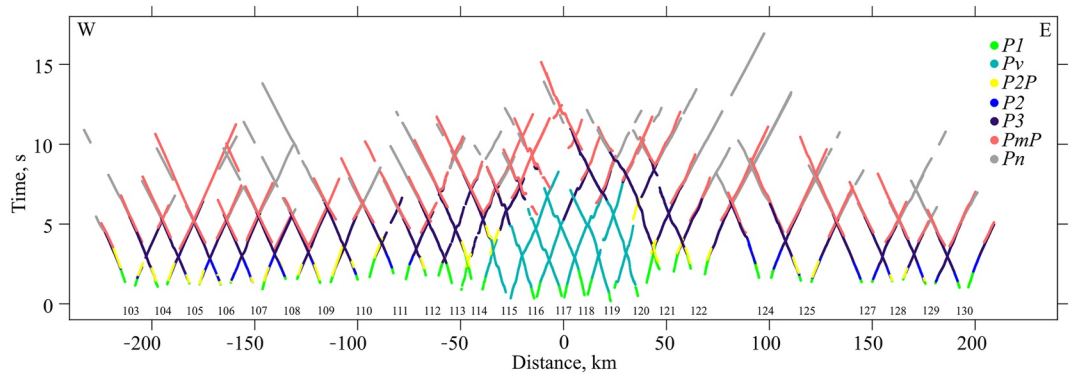


**Figure 4.** Travel-time plot of seismic phases (colored by phase) picked at each ocean-bottom-seismograph (OBS) station. Travel times are plotted with distance based on the stations position being the origin for each set of curves. Left trending phases represent shots fired from the west of the station and right trending phases represent shots from the east. The shot-receiver ranges are divided by two for better seismic phase alignment.

sections. Variations in the amplitude and separation of *PmP* and *Pn* phases indicate that the character of the Moho is variable along the seismic line. Away from Jimmu guyot, consistent *P*3-*Pn* cross-over distances of ~30–35 km suggests a relatively homogeneous and constant thickness oceanic crust.

For stations and shots located across the flexural moats that flank the edifice, the recordings show progressive delays as the edifice is approached (Figures 3b and 3e). *P*1 increases in total range to ~10 km, while *P*2 is delayed and clearly situated behind *P*1 as a secondary arrival, which suggests a thickened sedimentary layer in the moat. The *P*2*P*, *P*2, *P*3, *PmP*, and *Pn* phases are all also delayed, presumably due to the sediment layer thickening toward the edifice. Moreover, the *P*3-*Pn* cross-over distances for the western branch of OBS 113 (Figure 3b) and the eastern branch of OBS 122 (Figure 3e) increase to ~40–45 km, suggesting a commensurate deepening of the Moho. For shots on the opposite side of these two stations, which cross-over the edifice, there are large delays in the deeper arrivals, indicating significant crustal thickening.

For stations located on the flanks (Figure 3c) and the top (Figure 3d) of the edifice, the records shift earlier in time due to the reduced water column height, and the wave arrivals are affected by variable topography and subsurface velocity structures. The *P*1 arrivals indicate a varying sediment layer thickness. Furthermore, a new phase with crust-like apparent velocities (4–7 km/s) is observed that extends to much larger offsets than phases observed in oceanic crust away from the edifice. It emerges with a position in the records that indicates these waves turn at depths below the shallow low-velocity layer, but above the oceanic crust, such that it appears as a refraction turning above the reflector indicated by the *P*2*P* arrivals. This phase is a refraction that occurs throughout the edifice, which we designate as *Pv*. Changes in apparent velocity of *Pv* (e.g., Figures 3c and 3d) suggest considerable velocity variations with depth within the edifice. Moreover, the *Pv*/*P*3-*Pn* cross-over distances increase up to ~50 km on the summit of the edifice, indicating a deeper crust-mantle boundary or Moho beneath the edifice. Correspondingly, *PmP* arrivals shift to larger source-receiver offsets and times. In some instances, records show high-amplitude secondary phases at shorter offsets that look like standard *PmP* arrivals (e.g., western and eastern branch of OBS 118, Figure 3c), but shot-receiver reversal comparisons and modeling determined that they were not. The timing of these arrivals is consistent with a strong triplication or reflection from the top and sides of the high-velocity inner core of the edifice. Herein, we do not explicitly model these arrivals, but the refracted phases do capture the transition in velocities in the tomographic image.

Pick uncertainties were assigned manually based on the data quality and signal-to-noise ratio (Zelt & Forsyth, 1994). For sediment (*P*1) and upper crustal (*P*2) phases, the arrivals were picked to ±10–20 ms. Travel times of reflections from the upper reflector (*P*2*P*) were picked with uncertainties of ±30–40 ms. For larger offsets, the signal-to-noise ratio decreased, and lower crustal (*P*3) and the edifice (*Pv*) arrivals were picked to ±20–30 ms. Travel times of reflections from the crust-mantle boundary (*PmP*) and uppermost mantle (*Pn*) were picked with uncertainties of ±40–70 ms. Approximately 20,000 travel times were used in the tomographic analysis. All of the travel time picks for the various seismic phases are shown in Figure 4, which shows a clear pattern near the edifice of increasing time for the *PmP* phases and the presence of the *Pv* phases.

### 3.2. Gravity Data

Gravity data were acquired throughout cruise MGL1902, including along Lines OB01 and OB02. Data acquired along the transit from the Hawaiian Ridge to the Jimmu-Suiko guyots and along the 400-km-long north-south "strike" profile (Line OB02; Figure 1) are analyzed in Watts et al. (2020, 2021). In this study, we analyze the gravity data from the 495-km-long east-west "dip" profile that spatially correlates with our seismic line (Line OB01; Figure 1).

Gravity data were acquired with an axially constrained BGM-3 sensor (Bell & Watts, 1986) mounted on a gyrostabilized platform. In June 2018, the sensor was replaced, and the instrument recalibrated with a new pulse rate count to mGal conversion factor of 5.096606269 mGal/count and bias of 852513.49 mGal using tie-in data between the BGM-3 gravimeter and the Honolulu Alpha absolute gravity station. Tie-in data since June 2018 indicate that the new sensor system has performed well with a mistie at the start MGL1902 (some 310 days later) of +9.75 mGal and small drift rate during MGL1902 of −0.0744 mGal/day (Watts et al., 2020).

Prior to correcting for latitude and the Eötvös effect, the converted count data were filtered with a 120 s Gaussian filter, as recommended by the manufacturer (Bell Aerospace), in order to remove accelerations on the sensor due to ship motions. While such a filter is highly effective at removing swell "noise," we found there was still significant noise at high frequencies (short periods), albeit with much less power (Watts et al., 2020). We therefore applied an additional filter using a median filter (width = 0.5 km) which significantly reduced the high frequency noise and extended the overall decrease in power with increasing frequency seen in spectral data at low frequencies. We analyze the free-air gravity anomaly calculated from these data.

## 4. Seismic Methods

A nonlinear joint refraction and reflection travel time tomographic technique (Dunn et al., 2005) was used to solve for the *P* wave velocity structure of the sediments, crust, and upper mantle, and for the geometry of two reflectors: the top of oceanic crust and the crust-mantle interface. Because the method only allows one reflector at a time, the inversion was performed in two stages: one for the upper part of the model ("upper model") and one for the full model. For the upper model, the reflector was set at the presumed top of the oceanic crust, with the region above the reflector assumed to be comprised of the sediment layer and the edifice structure. For the full model, the upper reflector was removed, and a deeper reflector was positioned at the crust-mantle interface.

For the forward problem, the grid spacing was 250 m laterally and 100 m vertically. For the inverse problem the perturbation grid spacing was 2–4 km laterally and increased vertically from 0.2 km at the top to 1 km at the bottom vertically for the upper model. The vertical grid spacing of the full model increased from 0.2 km at the top to 2 km at the bottom. For ray tracing, we used a 3-D model to avoid artifacts due to the modest noncollinearity of the seismic line and stations, and possible out-of-plane effects due to local seafloor topography. The imaging itself was restricted to 2-D velocity and reflector variations within a vertical plane. For inversion, a priori uncertainties were applied to the model slowness and interface depth that act as damping terms to model perturbations, and spatial smoothness constraints were included to improve the solution stability and avoid statistical overfitting (Dunn et al., 2005).

For the upper model, *P2P* reflections, and *P*1, *Pv*, *P*2, and *P*3 refraction data were used for the inversion. We first constructed a 1-D depth-varying velocity model (Figure S4 in Supporting Information S1) based on the seismic structure derived from the legacy two-ship experiment of the Hawaiian Ridge (Brocher & ten Brink, 1987; ten Brink & Brocher, 1987). This model was used to solve for a 2-D solution, which was then averaged laterally to derive a new 1-D starting model. This procedure was repeated until changes of the 1-D starting model were insignificant. Using that model as a base, we formed 175 new starting models by adding depth perturbations of up to ±1.2 km to the initial reflector depth, and velocity perturbations of up to ±10% to the regions above and below the reflector. After completing the 175 solutions with each of the starting models, a final model (Figure 5) was obtained by calculating the mean of those models that achieved a $\chi^2$ (chi-square) misfit of less than one (157 out of 175 solutions). Data statistics for the final upper model are given in Table 1. Moreover, the final upper model (Figure 5) was converted to two-way travel time (TWTT) profile and compared with multichannel seismic reflection data, which shows good agreement (Figure S5 in Supporting Information S1).

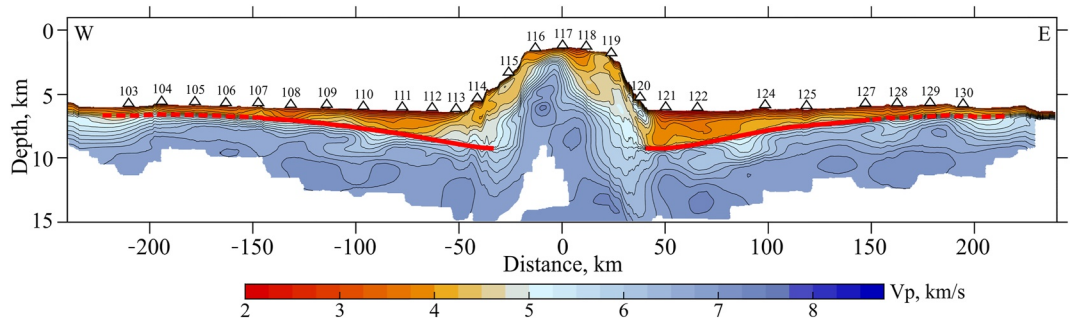


**Figure 5.** Upper layer tomographic image derived from averaging the solutions from 175 different starting models. Red lines indicate the average depth of the upper reflector, which we interpret as the top of the oceanic crust. Where the *P*2*P* picks were more subjective, the upper reflector was indicated by red dashed lines. This imaging used seismic phases *P*1, *Pv*, *P*2*P*, *P*2, and *P*3. The locations of ocean-bottom-seismographs (OBSs) are shown by white filled triangles.

For the full model, *PmP* reflections, and *P*1, *Pv*, *P*2, *P*3, and *Pn* refraction data were included in the inversion. The starting model consisted of the final 2-D model described above, with the region below the upper reflector replaced with the 1-D base model, a reflector at the crust-mantle interface, and a 1-D mantle region. As before, several iterations were performed to refine the base 1-D model, followed by perturbing this base model to generate a suite of starting models. Only the 1-D regions below the position of the upper reflector were varied in this manner. The depth perturbations for the lower reflector were up to ±2.25 km. After completing 125 solutions with each of the starting models, a final model (Figure 6a) was obtained by calculating the mean of those models that achieved a $\chi^2$ (chi-square) misfit of less than one (107 out of 125 solutions). Data statistics for the final model are given in Table 1. The uncertainties in the final averaged upper model and full model were assessed mainly in terms of the ray density and the standard deviation of the velocities and reflector depths, which are presented in Figures S6–S11 in Supporting Information S1. The largest uncertainties in V*p* occur in areas surrounding each reflector. This is due to a small trade-off between reflector depth and V*p* values that can occur within the uncertainty bounds of the *P*2*P* and *PmP* travel time picks, and these secondary phases tend to have larger assigned uncertainties than other types of picks. For the upper reflector, this trade-off is worse at larger distances from Jimmu guyot, where the sediment is thin and the *P*2*P* arrivals are sparse and have relatively large uncertainties.

## 5. Seismic Results

Figures 5 and 6a show the final images of upper and full models, respectively. They share a similar velocity structure above the upper reflector, so only the full model will be discussed except with regard to the upper reflector position and its uncertainty. The two OBS lines from this experiment cross at OBS 118 (Figure 1). A comparison of 1-D profiles at the intersection shows good agreement between them (Figure 7, solid and dashed red lines,

**Table 1**
*Misfits Between Travel Time Picks and Model Predictions*

| Upper model | *P*1, *Pv* | *P*2*P* | *P*2, *P*3 | Total |
|---|---|---|---|---|
| Number of picks | 3,006 | 942 | 6,750 | 10,698 |
| Final mean misfit (ms) | 1.21 | −4.37 | 0.11 | 0.02 |
| RMS misfit (ms) | 29.44 | 43.72 | 28.67 | 30.54 |
| $\chi^2$ | 1.03 | 1.20 | 0.87 | 0.94 |
| **Full model** | ***P*1, *Pv*, *P*2, *P*3** | ***PmP*** | ***Pn*** | **Total** |
| Number of picks | 9,401 | 6,498 | 4,560 | 20,459 |
| Final mean misfit (ms) | 3.92 | 7.56 | 8.02 | 5.99 |
| RMS misfit (ms) | 33.18 | 70.59 | 57.17 | 53.11 |
| $\chi^2$ | 0.92 | 1.05 | 0.90 | 0.96 |

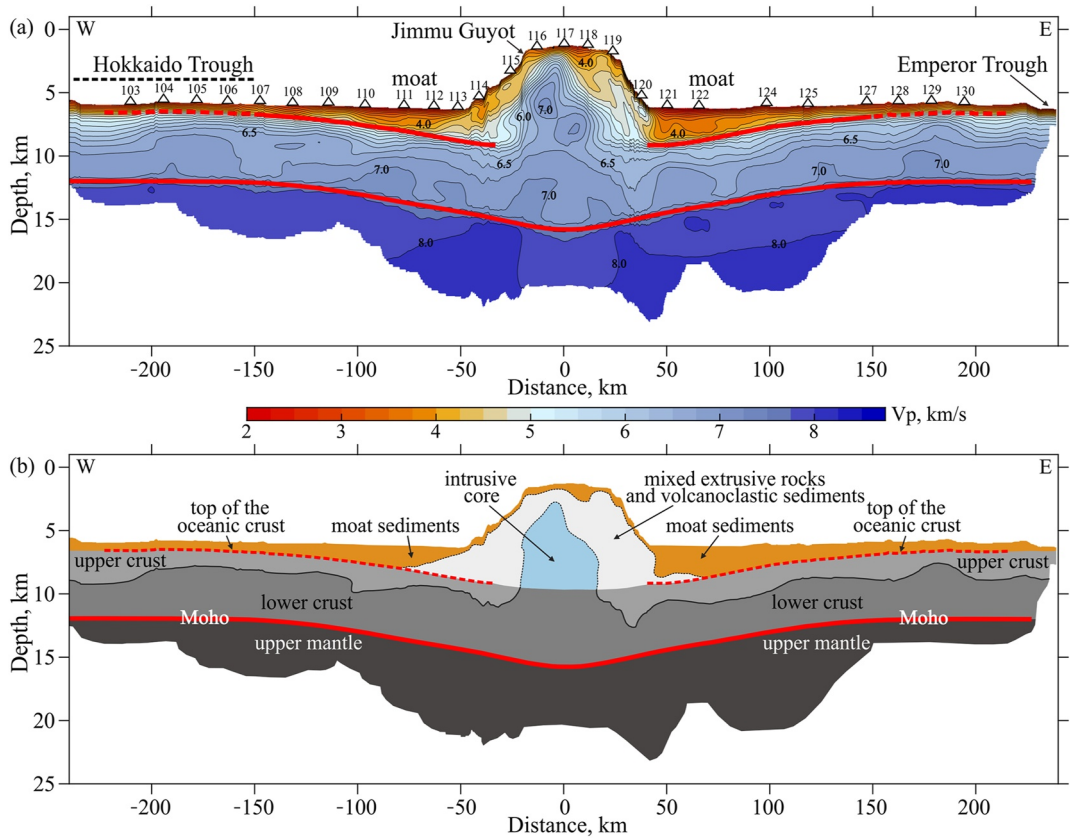


**Figure 6.** (a) Full crust and upper mantle tomographic image derived from averaging the solutions from 125 different starting models. The velocity contour interval is 0.25 km/s. Lower red solid line shows the average position of the lower reflector, which we interpret as the crust-mantle boundary (the upper red curve is from Figure 5). Imaging used *P*1, *Pv*, *P*2, *P*3, *PmP*, and *Pn* phases. The locations of ocean-bottom-seismographs (OBSs) are shown by white triangles. (b) Cartoon interpretation for volcanic edifice, oceanic crust, and upper mantle structures based on (a). Within the edifice, the sediment-extrusive boundary is based on the 4.0 km/s iso-velocity contour (Hammer et al., 1994; Weigel & Grevemeyer, 1999); the intrusive-extrusive boundary is based on the 6.0 km/s iso-velocity contour (Staudigel & Schmincke, 1984), and is compatible with the results in Watts et al. (2021). The upper-to-lower oceanic crustal boundary is based on the 6.5 km/s iso-velocity contour (Christeson et al., 2019). Red solid line indicates the average position of the Moho, and the upper red dashed lines show the average position of the top of the oceanic crust.

respectively). Our profile shows more small-scale variability, which may be due to differences in the methods used, including differences in the allowed vertical roughness of the models.

On oceanic crust away from Jimmu, the thickness of the sedimentary layer, as indicated by the subseafloor depth of the upper reflector, is ~0.4–0.7 km. At the ends of the seismic line where the reflector is quite shallow relative to the station spacing, the reflector position is the most uncertain, as are the velocities just above and below the reflector (see Supporting Information S1). Nevertheless, the sediment layer is relatively thin away from Jimmu and thickens into the moat toward the guyot.

In the moat areas, *P*2*P* reflections and *P*2 refractions indicate a dipping top of the oceanic crust and a thickening sedimentary layer toward the edifice. The thickness of the moat infill material is not symmetric on either side of Jimmu guyot, with up to ~1.7 km of material in the western moat (near the edge of the edifice) and up to ~2.6 km in the eastern moat (Figure 6a). It is expected that over the past ~120 Myr only about 0.2–0.3 km of the sediment was formed due to background pelagic sedimentation on the seafloor (Olson et al., 2016). Therefore, a large fraction of the moat infill (velocities of ~2.5–4.5 km/s) is likely due to the deposition of volcaniclastic sediments, and neighboring volcanic centers, including mass-wasting products derived from large-scale sector collapse of the flanks of Jimmu guyot.

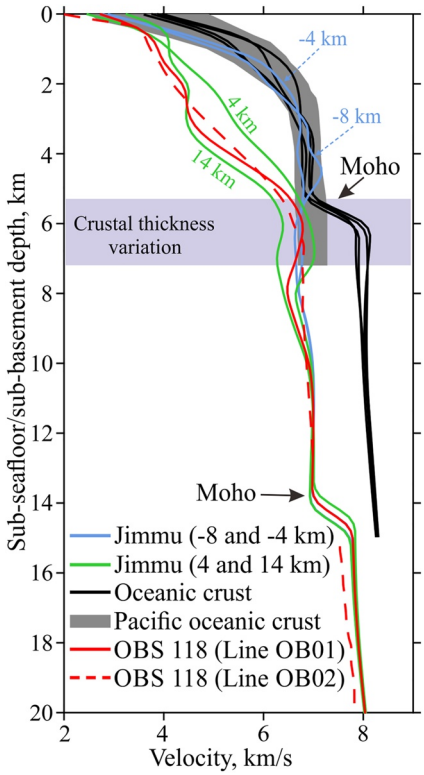


**Figure 7.** Comparison of 1-D velocity profiles for Jimmu guyot (solid blue, green, and red lines) and neighboring oceanic crust (solid black lines) to normal Pacific oceanic crust (gray shaded area) from Grevemeyer et al. (2018); and a comparison of profiles located at OBS 118 from this paper (solid red line) and the Watts et al. (2021) study (dashed red line). The solid blue lines are taken at distances of −8 and −4 km, while the solid green and red lines are taken at distances of 4, 11 (OBS 118), and 14 km along seismic Line OB01 (Figure 6a). The profiles for oceanic crust are constructed at distances of −210, −160, 160, and 210 km (Figure 6a). Purple area marks variation in crustal thickness for normal Pacific oceanic crust from Grevemeyer et al. (2018).

The low-velocity (<4 km/s) layer that caps the edifice shows lateral changes in thickness, with a general increase in thickness from the flanks to the summit, reaching up to ~1.5 km between OBSs 117 and 118 (Figure 6a). On the summit of Suiko guyot, the drill hole DSDP55-433 (Figure 1) indicated 163.0 m of sediments, underlain by 387.5 m of lava flows (Dalrymple et al., 1980). Thus, if the shallow structure of Jimmu and Suiko guyots are similar, we suggest that the low-velocity layer on the summit of the Jimmu is largely comprised of a thin sedimentary layer of pelagic material, coral reefs and limestone, overlying a relatively thick layer of mixed lava flows, dikes, and volcanoclastic and clastic debris.

Beneath the low-velocity layer, the velocity structure of the main body of the edifice can be divided into two parts: a lower-velocity exterior (*P* wave velocity (V*p*) ~4.0–6.0 km/s) and a higher-velocity interior (V*p* > 6.0 km/s) (Figure 6a). We interpret the exterior to be composed largely of extrusive volcanic material and debris flows formed during shield formation. The deeper burial of this material would be expected to close cracks and pores and give it a higher wave speed than the shallower material. This region is spatially highly heterogeneous with complicated velocity contours on both sides of the edifice. While this may be a general feature of high porosity extrusive basaltic rocks (Staudigel & Schmincke, 1984), it could also indicate large debris flows that were subsequently buried by lava flows during the shield-building stage of the volcano.

We interpret the interior of the edifice as largely composed of intrusive material. At ~1.6 km beneath OBS 117, the velocity is 6.0 km/s, and increases to 7.0 km/s at a depth of ~4.2 km (Figure 6a). At OBS 118, where the two OBS lines from this experiment cross, the 6.0 km/s iso-velocity contour is deeper (~4.5 km), in agreement with the velocity model in Watts et al. (2021; Figure 7). We believe the interior high-velocity structure indicates that the interior core of the edifice is largely comprised of intrusive mafic rocks (Hammer et al., 1994; Houtz & Ewing, 1976; Weigel & Grevemeyer, 1999), perhaps comprised of solidified feeder dikes, magma chambers, and mush zones. Beneath the central portion of the edifice there is no clear velocity discontinuity between the edifice material and the top of the oceanic crust (Figure 6). In addition, the low-velocity layer that is characteristic of the top of oceanic crust is missing beneath the edifice, presumably due to increasing overburden pressure and overprinting by new material that has intruded this region. Projecting the top of the reflector across this gap, then the height of the edifice above the oceanic crust is ~8.4 km and the width of the edifice is ~100–110 km. For the intrusive core, the height and width are ~6.7–6.9 and ~36–38 km, respectively (Figure 6a).

Within the oceanic crust in general (Figure 6a), the 6.5 km/s iso-velocity contour clearly marks the transition from a high gradient upper layer to a lower gradient lower layer, so we use the 6.5 km/s iso-velocity contour as a proxy for the upper-lower crustal boundary, which is consistent with the average velocity at the top of layer 3 for oceanic crust (Christeson et al., 2019). As compared to the west side, on the east side of the edifice the upper layer (~5.0–6.5 km/s) is slightly thicker (up to ~3.5-km thick beneath the east flank of the edifice) while the lower layer (~6.5–7.1 km/s) is slightly thinner. Beneath the moat and edifice, the 6.5 km/s iso-velocity contour is deflected first downward and then upward and approximately intersects with the 6.0 km/s iso-velocity contour within the edifice, indicating the disappearance of the upper-to-lower crustal boundary. Despite the depth uncertainties of the reflectors (Figure S11 in Supporting Information S1), the depth difference between them provides a proxy for the thickness of the oceanic crust (Figure S12 in Supporting Information S1). In general, the average thickness for the pre-existing oceanic crust is ~5.3 km along the seismic line.

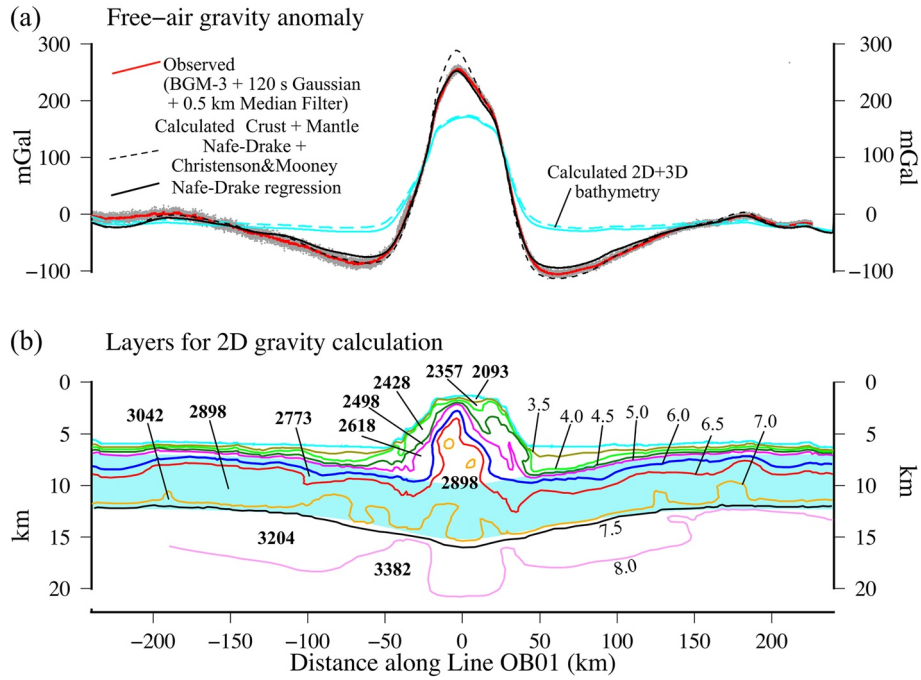


**Figure 8.** Comparison of the observed free-air gravity anomaly to the calculated gravity anomaly derived from the observed seismic structure along Line OB01. (a) Observed shipboard gravity data (gray filled circles and solid red line) and calculated gravity based on the empirical relationship between *P* wave velocity and density of Brocher (2005) which he derived from Nafe-Drake experimental data (solid black line) and a combination empirical relationship which he derived from the Nafe-Drake data for 2.0 < V*p* < 5.5 km/s and Christensen and Mooney (1995) for 5.5 < V*p* < 8.0 km/s (dashed black line). Light blue lines show the calculated two-dimensional and three-dimensional gravity effect of the bathymetry. (b) Iso-velocity contours derived from the tomographic image in Figure 6a that were used in the gravity calculations. Numbers to the right (light font) show the *P* wave velocity contour in km/s and numbers to the left (bold font) show the densities in kg/m$^3$ derived from the Nafe-Drake empirical relationship and used in the gravity modeling to determine the density contrast across each selected iso-velocity contour. The blue shaded area is the crustal structure derived from the flexural model assuming a thickness of the pre-flexed crust of 5.3 km (Figure S12 in Supporting Information S1), a density of the load, infill, crust, and mantle of 2,882, 2,510, 2,882, and 3,494 kg/m$^3$, respectively, and $T_e$ = 14 km.

Based on the depth of the lower reflector, which we interpret as the crust-mantle boundary, the Moho is depressed by ~3.8 km under the edifice, similar to the depression of the upper reflector when projected beneath the edifice. This deflection is attributed to volcano loading and subsequent plate flexure.

Away from the edifice, the structure of the upper mantle is not homogeneous. In the uppermost mantle beneath the edifice, within ~1 km of the Moho, wave speeds are generally lower than the average away from the edifice (~7.75 versus >7.9 km/s). Likewise, lower velocities were detected along the crossing seismic line (Watts et al., 2021), where the two profiles intersect. However, given the uncertainty of our image at this depth (~±0.2 km/s; see Supporting Information S1), this difference, and other variations across the top of the mantle, are not strongly supported.

## 6. Gravity Model

To verify the tomographic image in Figure 6a, we have computed the gravity effect of the seismically constrained crust and mantle structure and compared it to the observed gravity anomaly, assuming different empirical relationships between *P* wave velocity (V*p*) and density. Figure 8b shows the iso-velocity contours derived from Figure 6a and the densities derived from the empirical relationships that were used in the gravity calculations. The iso-velocity contours were selected that best defined the structure of the edifice and its flanking moats. The density was calculated from the average *P* wave in the "layer" bounding each iso-velocity contour assuming the empirical relationship derived by Brocher (2005) from a polynomial regression of both a field and experimental data set for sedimentary, metamorphic, and igneous rocks (Nafe & Drake, 1957), an updated version of which

was published in Ludwig et al. (1970). This so-called Nafe-Drake curve has been widely used to convert the *P* wave velocity derived from two-ship and sonobuoy global seismic refraction data sets (reviewed in Ludwig et al. (1970)) to density and to model the free-air gravity anomaly field over mid-ocean ridges, fracture zones and oceanic plateaus, and is generally believed (e.g., Brocher, 2005) to be applicable for $1.5 < Vp < 8.0$ km/s.

Figure 8a compares the observed and calculated free-air gravity anomalies along Line OB01. The observed anomaly is based on the measured 1 s BGM-3 count data acquired while R/V *Marcus G. Langseth* was shooting Line OB01. The count data were corrected for bias, converted to mGal, and filtered using a Gaussian filter of width 120 s (gray dots, Figure 8a) with an additional median filter of width 0.5 km (red solid line, Figure 8a). The calculated anomaly is based on 2-D line-integral and 3-D Fast Fourier Transform methods of quantifying the gravity effect of undulating interfaces. The figure shows a close agreement between the observed gravity anomaly and the calculated gravity anomaly based on the seismic tomographic model which is remarkable given that no adjustments have been made to the iso-velocity contours derived from the model in order to fit the gravity data. The gravity effects associated with individual iso-velocity contours are shown in Figure S13 in Supporting Information S1. The figure shows that the gravity effect of the bathymetry contributes to about 60% of the amplitude of the observed free-air gravity anomaly "high" over Jimmu guyot. The remainder of the "high" arises from the subseafloor structure, especially that associated with the 6.0 and 6.5 km/s refractors which we have interpreted as mainly intrusive material. The Root Mean Square (RMS) difference between the observed and calculated gravity in Figure 8a is 9.0 mGal, which is small compared to the wide range of free-air gravity anomalies that are observed (−100 to +250 mGal).

Although the calculated gravity based on the Nafe-Drake curve fits the observed gravity data over Jimmu guyot well, we have considered other possible empirical relationships between *P* wave velocity and density. For example, the dashed black line in Figure 8a shows the gravity anomaly that would be expected for the same iso-velocity contours in Figure 8b but a combination empirical relationship based on Nafe-Drake for $2.0 < Vp < 4.5$ km/s and Christensen and Mooney (1995) for $4.5 < Vp < 8.0$ km/s rather than just the Nafe-Drake empirical relationship. As Brocher (2005) pointed out, the Christensen and Mooney (1995) relationship predicts a density that is up to 150 kg/m$^3$ higher than the Nafe-Drake curve for $6.0 < Vp < 8.0$ km/s. The higher density should be reflected in the calculated gravity and the black dashed line in Figure 8a shows this to be the case over the crest of the guyot where the calculated gravity effect based on the combined Nafe-Drake and Christensen and Mooney (1995) empirical relationship is up to +34 mGal higher than the calculated anomaly based on just the Nafe-Drake empirical relationship. We note that the discrepancy is of a short wavelength and we were unable to negate it by decreasing, e.g., the density of the subcrustal mantle.

We caution that the gravity model in Figure 8 is based only on data acquired along Line OB01. The gravity calculations are based on a two-dimensional assumption since the extent of the iso-velocity contours either side of the line are unknown, except where the Line OB02 intersects it at OBS 118 (Figures 1 and 7). The bathymetry, however, is known from swath bathymetry data either side of Line OB01 and so we were able to compare the calculated gravity effect of the bathymetry in two-dimension and three-dimension. The comparison revealed an RMS difference of 2.0 mGal indicating that the effects due to subsurface three-dimensional structures may be small along Line OB01, at least in comparison to Line OB02 (Watts et al., 2021).

In summary, the gravity modeling reveals that the empirical relationship between *P* wave velocity and density derived by Brocher (2005) from an analysis of experimental data of Nafe and Drake (1957), updated in Ludwig et al. (1970), provides a satisfactory fit to both the seismic tomographic and gravity anomaly data acquired along Line OB01. Therefore, we conclude that the velocities and densities for the intrusive central "core" of the edifice are in the range 6.0–7.0 km/s and 2,733–2,898 kg/m$^3$ respectively and for the sediments and other material that infill the flanking flexural moats are in the range 2.5–5.0 km/s and 2,093–2,498 kg/m$^3$ respectively.

## 7. Discussion

The velocity model of the crust and upper mantle shown in Figure 6 enables new insights into the structure and formation of the Emperor Seamount Chain as well as that of the surrounding oceanic lithosphere. We will discuss the various aspects of the model related to oceanic crustal structure, edifice structure and evolution, volume flux, plate loading, and flexure in the following sections.

### 7.1. Oceanic Crustal Structure

Figure 7 shows a comparison between our results for the oceanic crust away from the edifice with the ensemble averages of Pacific oceanic crust from Grevemeyer et al. (2018). For better alignment, the variable sedimentary layer (~0.4–0.7 km) was removed in the 1-D velocity profiles of the oceanic crust. In general, the velocity-depth functions are in good agreement with average Pacific oceanic crust (Grevemeyer et al., 2018). The velocity increases from ~4 to ~6.5 km/s at a subbasement depth of ~1.9–2.1 km with a vertical velocity gradient of ~1.25 $s^{-1}$, and then to ~7.0 km/s at a depth of ~5.3 km with the smaller vertical velocity gradient of ~0.13 $s^{-1}$. The profiles suggest an oceanic crust thickness of ~5.3 km, which is at the low end of the variation in crustal thickness for normal Pacific oceanic crust (Grevemeyer et al., 2018). Similarly, along the crossing seismic Line OB02, Watts et al. (2021) suggested an estimate of ~5.1 km for the oceanic crustal thickness based on the integrated seismic and gravity models, which is consistent with our result.

Christeson et al. (2019) compiled a data set of global oceanic crustal structure from two-dimensional seismic profiles to explore differences related to spreading rate and age. They proposed that, for an old (>7.5 Ma) oceanic crust with a full-spreading rate of 80–160 mm/yr, the average thicknesses and standard deviations of upper crust (layer 2, mainly comprised of lava/dikes), lower crust (layer 3, mainly comprised of gabbro), and total oceanic crust are $1.97 \pm 0.56$, $4.15 \pm 0.99$, and $6.12 \pm 0.88$ km, respectively. In comparison, along seismic line OB01, the average thicknesses are ~2, ~3.3, and ~5.3 km for upper crust, lower crust, and total oceanic crust, respectively (Figures 6b, 7, and 8), indicating a similar upper crustal thickness but thinner lower and total crust compared to the global data set. In addition, our ~5.3-km-thick oceanic crust is also notably thinner than some other previous oceanic crustal thickness compilations (e.g., Dunn, 2015; White et al., 1992), and does not follow the average trend in the crustal thickness for the Pacific Ocean, which implies that the older crust should be thicker (Van Avendonk et al., 2017).

Recently, Ohira et al. (2017a) carried out an active-source seismic profile (>1,000-km long) near Koko guyot in the northwestern Pacific Ocean basin. The seafloor (128–148 Ma) along the line was formed at the Pacific-Farallon spreading ridge with a full rate of ~80 mm/yr. They estimated a thickness of ~5 km for oceanic crust, which is also thinner than normal Pacific oceanic crust. Hence, a possible explanation for the unusually thin oceanic crust along our seismic line as compared with previous compilations might be that, in the Pacific oceanic crust ensembles of Grevemeyer et al. (2018) and the global data set of Christeson et al. (2019), seismic profiles from the northwestern Pacific Ocean and the CNS area are under-represented. Moreover, some seismic experiments conducted in the Guatemala Basin (Ivandic et al., 2008) and on the Nazca Plate at ~43°S (Contreras-Reyes et al., 2007) also support thin Pacific oceanic crust (~5.0–5.5 km) and thus may indicate that regional differences in seafloor spreading or mantle composition and temperature (e.g., Dalton et al., 2014) may govern the observed variability.

In contrast to the oceanic crust away from the edifice, the low-velocity region at the top of the oceanic crust beneath the edifice is missing, as is the upper-to-lower crustal transition (Figure 6b), which perhaps indicates the oceanic crust has been modified by melts passing through, and perhaps crystallizing, in this region and/or by reduction in porosity due to the overlying edifice. Previous seismic studies of other seamounts and islands also reported the modified oceanic crust by magmatism, accompanied with an intrusive core within the edifice (e.g., Contreras-Reyes et al., 2010; Gallart et al., 1999; Weigel & Grevemeyer, 1999; Zucca et al., 1982). At the Louisville Ridge, e.g., Contreras-Reyes et al. (2010) imaged beneath the edifice a modified upper oceanic crust ($V_p$ ~7.0 km/s) and large-scale high-velocity intrusions in the lower oceanic crust ($V_p$ 7.2–7.6 km/s). The top of the oceanic crust and the upper-to-lower crustal boundary are also absent beneath the Louisville Ridge, indicating that magmatic intrusions penetrated both the upper and lower crust. While our image beneath Jimmu guyot also contains a modified upper crust, it does not show a large-scale high-velocity lower crust (at least not on the scale of the intracrustal magmatic intrusion at the Louisville Ridge). Instead there is a relatively normal-velocity lower oceanic crust ($V_p$ ~6.5–7.1 km/s; Figure 6).

### 7.2. Edifice Structure and Evolution

As described earlier, we interpret the volcanic edifice of Jimmu guyot as comprised of three parts: a very-low-velocity capping layer, an underlying thicker and moderately low-velocity layer, and a deeper higher-velocity core.

A priori observations from the area suggested that the capping layer is likely made up of a thin layer of pelagic material, coral reefs, and limestone, that overlie a relatively thick layer of mixed lava flows, dikes, and volcanoclastic debris (Dalrymple et al., 1980; Greene et al., 1978; Watts et al., 2021). A thin sedimentary layer is indirectly indicated by the dredge samples and drill hole recoveries (DSDP55-433) on Suiko guyot (Dalrymple et al., 1980), and by the seismic reflection result across the unnamed seamount between Jimmu and Suiko guyots (Greene et al., 1978; Watts et al., 2021). An underlying thicker layer of mixed lava flows, dikes, and volcanoclastic debris was also suggested by the drill hole DSDP55-433 (Dalrymple et al., 1980). Previous studies at other seamounts (e.g., Grevemeyer et al., 2001a; Hammer et al., 1994; Hill & Zucca, 1987; Watts & Masson, 1995; Weigel & Grevemeyer, 1999) related these low-velocity lithologies to debris flows or landslides occurring on the flanks and aprons of the edifice. Additionally, evidence from swath bathymetry data suggests Jimmu guyot has an approximately flat summit (Watts et al., 2021) and so has been wave-trimmed and was once at sea level. There is also evidence from the bathymetry at shallower depths than the wave-trimmed surface that it was subject to landsliding and down-slope sediment deposition. Consequently, we suggest that, as in the case of some other Emperor Seamounts (e.g., Suiko, Koko, and Daikakuji guyots), Jimmu guyot has progressed through stages of growth, erosion and wave-trimming, and subsidence that results in an eroded, submerged edifice that is flanked by a large amount of erosional debris (e.g., Smoot, 1982).

In Figure 7, we compared 1-D *P* wave velocity profiles for Jimmu guyot and oceanic crust along seismic Line OB01, along with normal Pacific oceanic crust (Grevemeyer et al., 2018). On the eastside of the summit (Figure 7, solid green and red lines), the profiles clearly indicate lower average velocity as compared to the oceanic crust in our study area and the normal Pacific oceanic crust at the equivalent depth (~1–5 km), consistent with the tomographic image along Line OB02 (Watts et al., 2021). Lower average velocities have also been detected at several other seamounts (e.g., Grevemeyer et al., 2001a; Hammer et al., 1994) and were interpreted as mixed extrusive rocks and volcanoclastic sediments with high porosities and low densities. In contrast, the west-central profiles (Figure 7, solid blue lines) suggest a significantly higher average velocity overlapping the oceanic crust and the normal Pacific oceanic crust, which we interpreted as the intrusive core comprised of intrusive gabbro or ultramafic rocks associated with the deep-water shield-building phase (e.g., Hammer et al., 1994; Staudigel & Schmincke, 1984; Watts et al., 2021; Weigel & Grevemeyer, 1999). The subseafloor depth of the intrusive core at its shallowest point is only ~1.5 km, which is much shallower than some other seamounts, e.g., the Jasper seamount (Hammer et al., 1994), the Great Meteor seamount (Weigel & Grevemeyer, 1999), and the island of La Reunion (Gallart et al., 1999), but resembles the island of Hawaii (Hill & Zucca, 1987; Zucca et al., 1982) and the Louisville guyot (Contreras-Reyes et al., 2010).

In general, along the seismic line, Jimmu guyot shows an obviously asymmetric structure: a greater degree of mixed extrusive rocks and volcanoclastic sediments are detected on the eastern part of the edifice, while the intrusive core is mainly located beneath the central-western part (Figure 6). Combined with the asymmetric thickness of volcaniclastic infill material of the flanking moats across Jimmu, where thicker sediments are observed to the east, we propose that, more destructive mass-wasting events (e.g., debris flows, sector collapses, or landslides) have occurred on the eastern rather than the western flank of the guyot during its formation and evolution. The shallow intrusive core within the edifice may have acted as a buttress and prevented sector collapses or landslides in the western part of Jimmu (e.g., Canales et al., 2000).

The extrusive-to-intrusive ratio is significant for understanding the predominant shield-building phase for Jimmu guyot. The cross-sectional area between the sediment-extrusive boundary (which we defined as the 4 km/s iso-velocity contour) and the top of the oceanic crust (Figure 6) is ~560 $km^2$, while the cross-sectional area of the intrusive core is ~160 $km^2$. Consequently, the area for the mixed extrusive basaltic rocks and volcanoclastic sediments is ~400 $km^2$, which gives an extrusive-to-intrusive ratio of ~2.5 and suggests that the Jimmu guyot was built mainly by extrusive magmatism, rather than intrusive processes. Moreover, the chosen sediment-extrusive boundary has excluded some area of oceanic basalts with a velocity of less than 4 km/s, which could lead to an underestimation of the extrusive area. Therefore, our estimate of the extrusive-to-intrusive ratio for Jimmu is rather conservative. Hammer et al. (1994) compared the velocity structures of Jasper seamount and Hawaii Island and found that although Jasper is far smaller than Hawaii, the thicknesses of the outer extrusive layer for both features are similar. Hence, they proposed that the extrusive-to-intrusive ratio is related to seamount or ocean island size. In contrast, at Louisville Ridge which is also smaller than Hawaii island, Contreras-Reyes et al. (2010) estimated an extrusive-to-intrusive ratio of only ~0.22, where the material within both the edifice

and oceanic crust is considered intrusive. They concluded that the Louisville Ridge grew dominantly by intrusive processes and the size of a seamount is not a controlling factor for extrusive-to-intrusive ratio. However, if the intrusions in the oceanic crust are excluded, the extrusive-to-intrusive ratio for the Louisville guyot is much larger (>1.2). Compared to the other three seamounts, Jimmu guyot is smaller than Hawaii Island, but larger than the Jasper seamount and the majority of the Louisville Ridge seamounts, and has a similarly thick (~2–5 km) extrusive layer covering the intrusive core. Therefore, our results are consistent with a possible relationship between seamount size and the extrusive-to-intrusive ratio. Ryan (1987) suggested that if the density equilibrium between the melts and surrounding edifice rocks dominantly control the structure of an active seamount, the intrusive level and magma chambers within the edifice will rise in response to new volcanic layers building up the seamount summit. This may explain the possible relationship between seamount size and the extrusive-to-intrusive ratio. Kaneda et al. (2010) proposed a possible model of formation processes of hotspot/mantle-derived seamounts and attributed the extrusive-to-intrusive ratio differences between different seamounts to their different formation stages. Based on this model, Jimmu guyot corresponds to an intermediate stage in which the magma was used mainly in the production of a large amount of extrusives, which leads in turn to a larger extrusive-to-intrusive ratio.

### 7.3. Volume Flux, Plate Loading, and Flexure

By combining the cross-sectional area of Jimmu's edifice and its along-strike length (~90–100 km), the volume of the volcanic material that has been added to the pre-existing oceanic crust can be estimated. In our estimation, the cross-sectional area of the edifice is assumed to be constant along strike, which gives an upper bound on the approximate total volume of $\sim 5.3 \times 10^4$ km$^3$ for magmatic material above the top of the oceanic crust at Jimmu. During the building of Jimmu guyot, the rate of age progression is ~5.7 cm/yr (O'Connor et al., 2013), which means that it took ~1.75 Myr to form the guyot and hence gives a volume flux of ~0.96 m$^3$/s using our volume estimate. This value is only half of the ~2 m$^3$/s estimated by Van Ark and Lin (2004) using gravity data and is significantly smaller than the estimates for the Hawaiian Ridge (Wessel, 2016). Along the 400-km-long Line OB02, Watts et al. (2021) obtained a volume flux of 0.56–0.68 m$^3$/s for the Emperor Seamounts, which is smaller than our estimate but still reasonable considering that their estimate includes both Jimmu and Suiko guyots and the intervening region. Previous studies have attempted to explain the marked changes of the volume flux along the Hawaiian-Emperor Seamount Chain in terms of changes in the dynamics of the Hawaiian plume. For example, using bathymetry data and considering plate flexure, Wessel (2016) evaluated the volume flux along the Hawaiian Ridge, and suggested that the long-period (10–15 Myr) and short-period (1–2 Myr) variations in the Hawaiian plume flux may be related to plate kinematic changes and plume-plate flexural interactions, respectively. By analyzing the relationship between radiogenic Pb with volume flux, Harrison et al. (2017) proposed that the movement of the deep source of the Hawaiian plume through different lower mantle compositional domains could affect the volume flux. Combining the plate reconstruction, geochemistry, and numerical modeling methods, Sun et al. (2021) suggested that the variation in volume flux could be explained by a plume-ridge interaction during the early evolution of the seamount chain. In summary, our new constraints on edifice size and structure from this study suggest that magmatic fluxes in the Emperor Seamount Chain are lower than previously estimated (Van Ark & Lin, 2004), and consistent with the results of Watts et al. (2021).

The seismic tomographic model can be used, together with bathymetry and gravity data, to constrain the flexure caused by submarine volcano loading and the elastic parameters associated with this flexure. Watts et al. (2021), e.g., used the load defined by the present-day bathymetry, together with the seismically constrained depth to Moho along Line OB02, to determine a best fit effective elastic thickness, $T_e$, of 14 km and thickness of the pre-flexed oceanic crust, $T_c$, of 5.1 km at Jimmu guyot, assuming a load density, $\rho_l$, and infill density, $\rho_{infill}$, of 2,882 kg/m$^3$. We have used a similar model ($T_e$ = 14 km) to calculate the flexure along Line OB01, except that we assumed $T_c$ = 5.3 km, which reflects our average thickness of oceanic crust away from the guyot, and a $\rho_{infill}$ = 2,510 kg/m$^3$, which reflects that Line OB01 traverses both the edifice where the infill density will be relatively high and the flexural moats where the infill density will be relatively low. Figure 8b (light blue shaded region) shows that a simple model of flexure based on this parameter pair explains well the seismically constrained average depth to both the top and base of oceanic crust and the Moho.

In summary, we estimate a relatively low $T_e$ of 14 km to explain the flexure observed beneath Jimmu guyot. Given the likely age of the oceanic plate at the time of volcanic emplacement (~55 Myr), our results are consistent

with global compilations which show that $T_e$ is a function of age of the plate at the time of loading (e.g., Watts & Zhong, 2000) and is given by the depth to the 450 °C oceanic isotherm based on plate cooling models. The main limitations with the model presented here concern the effect of subsurface loads such as the high *P* wave velocity (6.0–6.5 km/s) and density (2,773–2,898 kg/m$^3$) body that makes up the intrusive edifice core and the effect of lateral changes in the infill density, neither of which have been considered in the flexure modeling. These limitations may be addressed, in part, by the joint integration of seismic and gravity data along both Lines OB01 and OB02, but this is outside of the scope of the present paper.

Moreover, based on our seismic image, we do not see any evidence for large-scale magmatic underplating beneath the pre-existing oceanic crust which was reported by Watts et al. (1985) and ten Brink and Brocher (1987) at the Hawaiian Ridge in the vicinity of Oahu and Molokai, Caress et al. (1995) at Marquesas hotspot chain, Gallart et al. (1999) at La Reunion Island, and Grevemeyer et al. (2001a) at Ninetyeast Ridge.

## 8. Summary and Conclusions

We analyzed refraction and reflection OBS data along a 495-km-long east-west line that intersected the Emperor Seamount Chain at Jimmu guyot, and imaged the structure of the edifice and the underlying Pacific oceanic crust and upper mantle using *P* wave tomography. Our major findings are

1. We estimate a thickness for CNS oceanic crust of ~5.3 km, which is low compared to previous Pacific-wide oceanic crustal thickness compilations.
2. Jimmu guyot comprises a thin low-velocity capping layer of sediments and reef material, a thicker and moderately low-velocity layer of mixed extrusive rocks and volcanoclastic sediments, and a relatively high-velocity core of intrusive gabbro or ultramafic rock.
3. Beneath the edifice, the low-velocity region that characterizes upper oceanic crust is missing, which suggests modification of oceanic crust by melts passing through or crystallizing. No significant modification of the lower crust was detected.
4. The asymmetric distribution of intrusive core and extrusive rocks in the edifice and volcanoclastic sediments in the flanking moats suggests that more destructive mass-wasting events occurred on the eastern flank of Jimmu guyot during its formation. The intrusive core may have acted as a buttress and prevented the occurrence of sector collapses or landslides to the west.
5. The extrusive-to-intrusive ratio is ~2.5, which suggests that the edifice was built mainly by extrusive, rather than intrusive processes.
6. No extensive magmatic underplating of the pre-existing oceanic crust is present.
7. We estimate a total volume of ~$5.3 \times 10^4$ km$^3$ for magmatic material that has been added to the surface of the pre-existing Pacific oceanic crust, and a volume flux of ~0.96 m$^3$/s during the formation of Jimmu guyot. Our estimation of the volume flux is significantly smaller than some previous studies, but consistent with the estimates from an intersecting along-strike seismic line (Watts et al., 2021).
8. Volcanic loading has depressed the pre-existing Pacific oceanic crust by ~3.8 km over a broad (~300-km wide) region. Using a density model converted from the tomographic image, the plate flexure was modeled and indicates an effective elastic thickness of ~14 km for the Pacific plate.

## Data Availability Statement

We are grateful to the officers, crew, and scientific and technical staff onboard R/V *Marcus G. Langseth* for helping make the acquisition of the seismic, bathymetry, and gravity data used in this paper possible. Cruise data are archived at dx.doi.org/10.7284/908198. Seismic data were provided by instruments from the Ocean-Bottom Seismic Instrument Center (https://obsic.whoi.edu), which is funded by the National Science Foundation and provided by GEOMAR. The OBSIC seismic data are archived at the IRIS Data Management Center (http://service.iris.edu/fdsnws/dataselect/1/) and the GEOMAR seismic data are archived at PANGAEA (https://doi.org/10.1594/PANGAEA.941101).

**Acknowledgments**
This research was supported by the National Science Foundation grant OCE-1737243 to R. A. Dunn, OCE-1737245 to D. J. Shillington, and A. B. Watts. C. Xu was supported by the China Scholarship Council under Grant 201906330037. The data processing and manuscript writing were performed while the lead author was at the University of Hawaii at Manoa.

## References

Atwater, T., Sclater, J., Sandwell, D., Severinghaus, J., & Marlow, M. (1993). Fracture zone traces across the North Pacific Cretaceous Quiet Zone and their tectonic implications. In M. S. Pringle, W. W. Sager, W. V. Sliter, & S. Stein (Eds.), *The Mesozoic Pacific: Geology, Tectonics, and volcanism Geophysical Monograph 77* (pp. 137–154). American Geophysical Union. https://doi.org/10.1029/GM077p0137

Bell, R. E., & Watts, A. B. (1986). Evaluation of the BGM-3 sea gravity meter system onboard R/V Conrad. *Geophysics*, *51*(7), 1480–1493. https://doi.org/10.1190/1.1442196

Boston, B., Shillington, D. J., Dunn, R. A., Watts, A. B., Grevemeyer, I., Gomez de la Pena, L., et al. (2019). *The crustal and upper mantle structure of the Hawaiian-Emperor Seamount Chain from marine seismic data*. American Geophysical Union, Fall Meeting 2019, Abstract #T41B-06.

Brocher, T. M. (2005). Empirical relations between elastic wavespeeds and density in the Earth's crust. *Bulletin of the Seismological Society of America*, *95*(6), 2081–2092. https://doi.org/10.1785/0120050077

Brocher, T. M., & ten Brink, U. S. (1987). Variations in oceanic layer 2 elastic velocities near Hawaii and their correlation to lithospheric flexure. *Journal of Geophysical Research*, *92*(B3), 2647–2661. https://doi.org/10.1029/JB092iB03p02647

Calmant, S. (1987). The elastic thickness of the lithosphere in the Pacific Ocean. *Earth and Planetary Science Letters*, *85*(1), 277–288. https://doi.org/10.1016/0012-821X(87)90038-0

Canales, J. P., Dañobeitia, J. J., & Watts, A. B. (2000). Wide-angle seismic constraints on the internal structure of Tenerife, Canary Islands. *Journal of Volcanology and Geothermal Research*, *103*(1–4), 65–81. https://doi.org/10.1016/S0377-0273(00)00216-X

Caress, D. W., McNutt, M. K., Detrick, R. S., & Mutter, J. C. (1995). Seismic imaging of hotspot-related crustal underplating beneath the Marquesas Islands. *Nature*, *373*(6515), 600–603. https://doi.org/10.1038/373600a0

Charvis, P., Laesanpura, A., Gallart, J., Hirn, A., Lépine, J. C., deVoogd, B., et al. (1999). Spatial distribution of hotspot material added to the lithosphere under La Réunion, from wide-angle seismic data. *Journal of Geophysical Research*, *104*(B2), 2875–2893. https://doi.org/10.1029/98JB02841

Chase, T. E., Menard, H. W., & Mammerickx, J. (1968). *Bathymetry of the North Pacific*. Scripps Institution of Oceanography.

Christensen, N. I., & Mooney, W. D. (1995). Seismic velocity structure and composition of the continental crust: A global view. *Journal of Geophysical Research*, *100*(B6), 9761–9788. https://doi.org/10.1029/95JB00259

Christeson, G. L., Goff, J. A., & Reece, R. S. (2019). Synthesis of oceanic crustal structure from two-dimensional seismic profiles. *Reviews of Geophysics*, *57*, 504–529. https://doi.org/10.1029/2019RG000641

Clague, D. A., & Dalrymple, G. B. (1987). The Hawaiian-Emperor volcanic chain. Part I. Geologic evolution. *U. S. Geological Survey Professional Paper*, *1350*(1350), 5–54.

Contreras-Reyes, E., Grevemeyer, I., Flueh, E. R., Scherwath, M., & Heesemann, M. (2007). Alteration of the subducting oceanic lithosphere at the southern central Chile trench–outer rise. *Geochemistry, Geophysics, Geosystems*, *8*, Q07003. https://doi.org/10.1029/2007GC001632

Contreras-Reyes, E., Grevemeyer, I., Watts, A. B., Planert, L., Flueh, E. R., & Peirce, C. (2010). Crustal intrusion beneath the Louisville hotspot track. *Earth and Planetary Science Letters*, *289*(3–4), 323–333. https://doi.org/10.1016/j.epsl.2009.11.020

Dalrymple, G. B., Lanphere, M. A., & Clague, D. A. (1980). Conventional and $^{40}Ar/^{39}Ar$ K-Ar Ages of Volcanic Rocks from Ťjin (Site 430), Nintoku (Site 432), and Suiko (Site 433) Seamounts and the Chronology of Volcanic Propagation along the Hawaiian-Emperor Chain. *Initial Reports of the D.S.D.P.*, *55*, 659–676. https://doi.org/10.2973/dsdp.proc.55.128.1980

Dalton, C. A., Langmuir, C. H., & Gale, A. (2014). Geophysical and geochemical evidence for deep temperature variations beneath mid-ocean ridges. *Science*, *344*(6179), 80–83. https://doi.org/10.1126/science.1249466

Den, N., Ludwig, W. J., Murauchi, S., Ewing, J. I., Hotta, H., Edgar, N. T., et al. (1969). Seismic-refraction measurements in the northwest Pacific basin. *Journal of Geophysical Research*, *74*(6), 1421–1434. https://doi.org/10.1029/JB074i006p01421

Dietz, R. S. (1954). Marine geology of northwestern pacific: Description of Japanese bathymetric chart 6901. *The Geological Society of America Bulletin*, *65*(12), 1199–1224. https://doi.org/10.1130/0016-7606(1954)65[1199:MGONPD]2.0.CO;2

Doubrovine, P. V., Steinberger, B., & Torsvik, T. H. (2012). Absolute plate motions in a reference frame defined by moving hot spots in the Pacific, Atlantic, and Indian oceans. *Journal of Geophysical Research*, *117*, B09101. https://doi.org/10.1029/2011JB009072

Duncan, R. A., & Keller, R. A. (2004). Radiometric ages for basement rocks from the Emperor Seamounts, ODP Leg 197. *Geochemistry, Geophysics, Geosystems*, *5*, Q08L03. https://doi.org/10.1029/2004GC000704

Dunn, R. A. (2015). Crust and lithospheric structure-seismic structure of mid-ocean ridges. In A. Dziewonski, & B. Romanowicz (Eds.), *Treatise on geophysics* (pp. 419–451). https://doi.org/10.1016/B978-0-444-53802-4.00011-7

Dunn, R. A., Arai, R., Eason, D. E., Canales, J. P., & Sohn, R. A. (2017). Three-dimensional seismic structure of the mid-Atlantic ridge: An investigation of tectonic, magmatic, and hydrothermal processes in the rainbow area. *Journal of Geophysical Research: Solid Earth*, *122*, 9580–9602. https://doi.org/10.1002/2017JB015051

Dunn, R. A., & Hernandez, O. (2009). Tracking blue whales in the eastern tropical Pacific with an ocean-bottom seismometer and hydrophone array. *Journal of the Acoustical Society of America*, *126*(3), 1084–1094. https://doi.org/10.1121/1.3158929

Dunn, R. A., Lekić, V., Detrick, R. S., & Toomey, D. R. (2005). Three-dimensional seismic structure of the Mid-Atlantic Ridge (35°N): Evidence for focused melt supply and lower crustal dike injection. *Journal of Geophysical Research*, *110*, B09101. https://doi.org/10.1029/2004JB003473

Erickson, B. H., Naugler, F. P., & Lucas, W. H. (1970). Emperor fracture zone: A newly discovered feature in the central north Pacific. *Nature*, *225*(5227), 53–54. https://doi.org/10.1038/225053a0

Farrar, E., & Dixon, J. M. (1981). Early tertiary rupture of the Pacific plate: 1700 km of dextral offset along the Emperor trough-line islands lineament. *Earth and Planetary Science Letters*, *53*(3), 307–322. https://doi.org/10.1016/0012-821X(81)90036-4

Furukawa, K., Gettrust, J. F., Kroenke, L. W., & Campbell, J. F. (1980). Crust and upper mantle structure along the flank of Kōko Seamount. *Bulletin of the Seismological Society of America*, *70*(4), 1161–1169. https://doi.org/10.1785/BSSA0700041161

Gallart, J., Driad, L., Charvis, P., Sapin, M., Hirn, A., Diaz, J., et al. (1999). Perturbation to the lithosphere along the hotspot track of La Réunion from an offshore-onshore seismic transect. *Journal of Geophysical Research*, *104*(B2), 2895–2908. https://doi.org/10.1029/98JB02840

Gordon, R. G. (1982). Paleomagnetic test of the Emperor fracture zone hypothesis. *Geophysical Research Letters*, *9*(11), 1283–1286. https://doi.org/10.1029/GL009i011p01283

Green, J. A., & Fleischer, P. (1980). *Environmental report on the northwest Pacific for the marine seismic system (MSS) Rep*. National Space Technology Laboratory Station, Mississippi: Naval Ocean Research and Development Activity.

Greene, H. G., Dalrymple, G. B., & Clague, D. A. (1978). Evidence for northward movement: Of the Emperor Seamounts. *Geology*, *6*(2), 70–74. https://doi.org/10.1130/0091-7613(1978)6<70:EFNMOT>2.0.CO;2

Grevemeyer, I., & Flueh, E. R. (2000). Crustal underplating and its implications for subsidence and state of isostasy along the Ninetyeast Ridge hotspot trail. *Geophysical Journal International*, *142*(2), 643–649. https://doi.org/10.1046/j.1365-246x.2000.00154.x

Grevemeyer, I., Flueh, E. R., Reichert, C., Bialas, J., Kläschen, D., & Kopp, C. (2001a). Crustal architecture and deep structure of the Nine-tyeast Ridge hotspot trail from active-source ocean bottom seismology. *Geophysical Journal International*, *144*(2), 414–431. https://doi.org/10.1046/j.0956-540x.2000.01334.x

Grevemeyer, I., Ranero, C. R., & Ivandic, M. (2018). Structure of oceanic crust and serpentinization at subduction trenches. *Geosphere*, *14*(2), 395–418. https://doi.org/10.1130/GES01537.1

Grevemeyer, I., Weigel, W., Schüssler, S., & Avedik, F. (2001b). Crustal and upper mantle seismic structure and lithospheric flexure along the Society Island hotspot chain. *Geophysical Journal International*, *147*(1), 123–140. https://doi.org/10.1046/j.0956-540x.2001.01521.x

Hammer, P. T. C., Dorman, L. M., Hildebrand, J. A., & Cornuelle, B. D. (1994). Jasper Seamount structure: Seafloor seismic refraction tomography. *Journal of Geophysical Research*, *99*(B4), 6731–6752. https://doi.org/10.1029/93JB02170

Harding, A. J., Kent, G. M., & Orcutt, J. A. (1993). A multichannel seismic investigation of upper crustal structure at 9°N on the East Pacific Rise: Implications for crustal accretion. *Journal of Geophysical Research*, *98*(B8), 13925–13944. https://doi.org/10.1029/93JB00886

Harrison, L. N., Weis, D., & Garcia, M. O. (2017). The link between Hawaiian mantle plume composition, magmatic flux, and deep mantle geodynamics. *Earth and Planetary Science Letters*, *463*, 298–309. https://doi.org/10.1016/j.epsl.2017.01.027

Hilde, T. W. C., Uyeda, S., & Kroenke, L. (1977). Evolution of the Western Pacific and its margin. *Tectonophysics*, *38*(1), 145–165. https://doi.org/10.1016/0040-1951(77)90205-0

Hill, D. P., & Zucca, J. J. (1987). Geophysical constraints on the structure of Kilauea and Mauna Loa volcanoes and some implications for seismomagmatic processes. *U. S. Geological Survey Professional Paper*, *1350*(2), 903–917.

Houtz, R. E. (1976). Seismic properties of layer 2A in the Pacific. *Journal of Geophysical Research*, *81*(35), 6321–6331. https://doi.org/10.1029/JB081i035p06321

Houtz, R. E., & Ewing, J. I. (1976). Upper crustal structure as a function of plate age. *Journal of Geophysical Research*, *81*(14), 2490–2498. https://doi.org/10.1029/JB081i014p02490

Ivandic, M., Grevemeyer, I., Berhorst, A., Flueh, E. R., & McIntosh, K. (2008). Impact of bending related faulting on the seismic properties of the incoming oceanic plate offshore of Nicaragua. *Journal of Geophysical Research*, *113*, B05410. https://doi.org/10.1029/2007JB005291

Jackson, E., Koisumi, I., Dalrymple, G., Clague, D., Kirkpatrick, R., & Greene, H. (1980). Introduction and summary of results from DSDP Leg 55, the Hawaiian-Emperor hot-spot experiment. In E. D.Jackson, I.Koizumi, G.Brent Dalrymple, D. A.Clague, R.James Kirkpatrick, & H.Gary Greene (Eds.), *Initial Reports of the Deep Sea drilling Project* (pp. 5–31). Washington, DC: US Government Printing Office. https://doi.org/10.2973/dsdp.proc.55.101.1980

Kaneda, K., Kodaira, S., Nishizawa, A., Morishita, T., & Takahashi, N. (2010). Structural evolution of preexisting oceanic crust through intraplate igneous activities in the Marcus-Wake seamount chain. *Geochemistry, Geophysics, Geosystems*, *11*, Q10014. https://doi.org/10.1029/2010GC003231

Kerr, B. C., Scholl, D. W., & Klemperer, S. L. (2005). Seismic stratigraphy of Detroit Seamount, Hawaiian-Emperor Seamount Chain: Post-hot-spot shield-building volcanism and deposition of the Meiji drift. *Geochemistry, Geophysics, Geosystems*, *6*, Q07L10. https://doi.org/10.1029/2004GC000705

Kopp, H., Kopp, C., Phipps Morgan, J., Flueh, E. R., Weinrebe, W., & Morgan, W. J. (2003). Fossil hot spot-ridge interaction in the Musicians Seamount Province: Geophysical investigations of hot spot volcanism at volcanic elongated ridges. *Journal of Geophysical Research*, *108*(B3), 2160. https://doi.org/10.1029/2002JB002015

Larson, R. L., & Chase, C. G. (1972). Late mesozoic evolution of the Western Pacific ocean. *Geological Society of America Bulletin*, *83*(12), 3627–3644. https://doi.org/10.1130/0016-7606(1972)83[3627:LMEOTW]2.0.co;2

Lindwall, D. A. (1988). A two-dimensional seismic investigation of crustal structure under the Hawaiian Islands near Oahu and Kauai. *Journal of Geophysical Research*, *93*(B10), 12107–12122. https://doi.org/10.1029/JB093iB10p12107

Ludwig, W. J., Nafe, J. E., & Drake, C. L. (1970). 2. Seismic refraction. In A. Maxwell (Ed.), *The sea* (pp. 53–84). New York: Interscience.

Mammerickx, J., & Sharman, G. F. (1988). Tectonic evolution of the North Pacific during the Cretaceous quiet period. *Journal of Geophysical Research*, *93*(B4), 3009. https://doi.org/10.1029/JB093iB04p03009

McNutt, M. (1984). Lithospheric flexure and thermal anomalies. *Journal of Geophysical Research*, *89*(B13), 11180–11194. https://doi.org/10.1029/JB089iB13p11180

McNutt, M., & Bonneville, A. (2000). A shallow, chemical origin for the Marquesas Swell. *Geochemistry, Geophysics, Geosystems*, *1*(6), 1014. https://doi.org/10.1029/1999GC000028

Meléndez, A., Sallarès, V., Ranero, C. R., & Kormann, J. (2014). Origin of water layer multiple phases with anomalously high amplitude in near-seafloor wide-angle seismic recordings. *Geophysical Journal International*, *196*(1), 243–252. https://doi.org/10.1093/gji/ggt391

Morgan, W. J. (1971). Convection plumes in the lower mantle. *Nature*, *230*(5288), 42–43. https://doi.org/10.1038/230042a0

Müller, R. D., Sdrolias, M., Gaina, C., & Roest, W. R. (2008). Age, spreading rates, and spreading asymmetry of the world's ocean crust. *Geochemistry, Geophysics, Geosystems*, *9*, Q04006. https://doi.org/10.1029/2007GC001743

Nafe, J. E., & Drake, C. L. (1957). Variations with depth in shallow and deep water marine sediments of porosity, density and the velocities of compressional and shear waves. *Geophysics*, *22*(3), 523–552. https://doi.org/10.1190/1.1438386

O'Connor, J. M., Steinberger, B., Regelous, M., Koppers, A. A. P., Wijbrans, J. R., Haase, K. M., et al. (2013). Constraints on past plate and mantle motion from new ages for the Hawaiian-Emperor Seamount Chain. *Geochemistry, Geophysics, Geosystems*, *14*, 4564–4584. https://doi.org/10.1002/ggge.20267

Ohira, A., Kodaira, S., Nakamura, Y., Fujie, G., Arai, R., & Miura, S. (2017). Structural variation of the oceanic Moho in the Pacific plate revealed by active-source seismic data. *Earth and Planetary Science Letters*, *476*, 111–121. https://doi.org/10.1016/j.epsl.2017.08.004

Olson, P., Reynolds, E., Hinnov, L., & Goswami, A. (2016). Variation of ocean sediment thickness with crustal age. *Geochemistry, Geophysics, Geosystems*, *17*, 1349–1369. https://doi.org/10.1002/2015GC006143

Parsons, B., & Sclater, J. G. (1977). An analysis of the variation of ocean floor bathymetry and heat flow with age. *Journal of Geophysical Research*, *82*(5), 803–827. https://doi.org/10.1029/JB082i005p00803

Pim, J., Peirce, C., Watts, A. B., Grevemeyer, I., & Krabbenhöft, A. (2008). Crustal structure and origin of the Cape Verde Rise. *Earth and Planetary Science Letters*, *272*(1–2), 422–428. https://doi.org/10.1016/j.epsl.2008.05.012

Rees, B. A., Detrick, R., & Coakley, B. J. (1993). Seismic stratigraphy of the Hawaiian flexural moat. *Geological Society of America Bulletin*, *105*(2), 189–205. https://doi.org/10.1130/0016-7606(1993)105<0189:SSOTHF>2.3.CO;2

Ryan, M. P. (1987). Neutral buoyancy and the mechanical evolution of magmatic systems. In B. O. Mysen (Ed.), *Magmatic process: Physicochemical principles* (pp. 259–287). Special Publication Geochemical Society.

Sallarès, V., Charvis, P., Flueh, E. R., & Bialas, J. (2003). Seismic structure of Cocos and Malpelo Volcanic Ridges and implications for hot spot-ridge interaction. *Journal of Geophysical Research*, *108*(B12), 2564. https://doi.org/10.1029/2003JB002431

Sallarès, V., Charvis, P., Flueh, E. R., Bialas, J., & the SALIERI Scientific Party. (2005). Seismic structure of the Carnegie ridge and the nature of the Galápagos hotspot. *Geophysical Journal International*, *161*(3), 763–788. https://doi.org/10.1111/j.1365-246X.2005.02592.x

Sandwell, D. T., Harper, H., Tozer, B., & Smith, W. H. F. (2019). Gravity field recovery from geodetic altimeter missions. *Advances in Space Research*, *68*, 1059–1072. https://doi.org/10.1016/j.asr.2019.09.011

Seton, M., Müller, R. D., Zahirovic, S., Gaina, C., Torsvik, T., Shephard, G., et al. (2012). Global continental and ocean basin reconstructions since 200Ma. *Earth-Science Reviews*, *113*(3–4), 212–270. https://doi.org/10.1016/j.earscirev.2012.03.002

Seton, M., Müller, R. D., Zahirovic, S., Williams, S., Wright, N. M., Cannon, J., et al. (2020). A global data set of present-day oceanic crustal age and seafloor spreading parameters. *Geochemistry, Geophysics, Geosystems*, *21*, e2020GC009214. https://doi.org/10.1029/2020GC009214

Sharp, W. D., & Clague, D. A. (2006). 50-Ma initiation of Hawaiian-Emperor bend records major change in Pacific plate motion. *Science*, *313*(5791), 1281–1284. https://doi.org/10.1126/science.1128489

Smoot, N. C. (1982). Guyots of the Mid-Emperor Chain mapped with multibeam sonar. *Marine Geology*, *47*(1), 153–163. https://doi.org/10.1016/0025-3227(82)90024-X

Smoot, N. C., & Lowrie, A. (1985). Emperor fracture zone morphology by multi-beam sonar. *The Journal of Geology*, *93*(2), 196–204. https://doi.org/10.1086/628941

Staudigel, H., & Schmincke, H.-U. (1984). The Pliocene seamount series of La Palma/Canary islands. *Journal of Geophysical Research*, *89*(B13), 11195–11215. https://doi.org/10.1029/JB089iB13p11195

Sun, W., Langmuir, C. H., Ribe, N. M., Zhang, L., Sun, S., Li, H., et al. (2021). Plume-ridge interaction induced migration of the Hawaiian-Emperor Seamounts. *Science Bulletin*, *66*, 1691–1697. https://doi.org/10.1016/j.scib.2021.04.028

Tarduno, J. A., Duncan, R. A., Scholl, D. W., Cottrell, R. D., Steinberger, B., & Thordarson, T. (2003). The Emperor Seamounts: Southward motion of the Hawaiian hotspot plume in Earth's mantle. *Science*, *301*(5636), 1064–1069. https://doi.org/10.1126/science.1086442

ten Brink, U. S., & Brocher, T. M. (1987). Multichannel seismic evidence for a subcrustal intrusive complex under Oahu and a model for Hawaiian volcanism. *Journal of Geophysical Research*, *92*(B13), 13687–13707. https://doi.org/10.1029/JB092iB13p13687

Tozer, B., Sandwell, D. T., Smith, W. H. F., Olson, C., Beale, J. R., & Wessel, P. (2019). Global bathymetry and topography at 15 arc sec: SRTM15+. *Earth and Space Science*, *6*, 1847–1864. https://doi.org/10.1029/2019EA000658

Van Ark, E., & Lin, J. (2004). Time variation in igneous volume flux of the Hawaii-Emperor hot spot seamount chain. *Journal of Geophysical Research*, *109*, B11401. https://doi.org/10.1029/2003JB002949

Van Avendonk, H. J. A., Davis, J. K., Harding, J. L., & Lawver, L. A. (2017). Decrease in oceanic crustal thickness since the breakup of Pangaea. *Nature Geoscience*, *10*(1), 58–61. https://doi.org/10.1038/ngeo2849

Vidal, V., & Bonneville, A. (2004). Variations of the Hawaiian hot spot activity revealed by variations in the magma production rate. *Journal of Geophysical Research*, *109*, B03104. https://doi.org/10.1029/2003JB002559

Walther, C. H. E. (2003). The crustal structure of the Cocos ridge off Costa Rica. *Journal of Geophysical Research*, *108*(B3), 2136. https://doi.org/10.1029/2001JB000888

Watts, A. B. (1978). An analysis of isostasy in the world's oceans 1. Hawaiian-Emperor Seamount Chain. *Journal of Geophysical Research*, *83*(B12), 5989–6004. https://doi.org/10.1029/JB083iB12p05989

Watts, A. B., & Cochran, J. R. (1974). Gravity anomalies and flexure of the lithosphere along the Hawaiian-Emperor Seamount Chain. *Geophysical Journal International*, *38*(1), 119–141. https://doi.org/10.1111/j.1365-246X.1974.tb04112.x

Watts, A. B., Grevemeyer, I., Shillington, D. J., Dunn, R. A., Boston, B., & Gómez de la Peña, L. (2021). Seismic structure, gravity anomalies and flexure along the Emperor Seamount Chain. *Journal of Geophysical Research: Solid Earth*, *126*, e2020JB021109. https://doi.org/10.1029/2020JB021109

Watts, A. B., & Masson, D. G. (1995). A giant landslide on the north flank of Tenerife, Canary Islands. *Journal of Geophysical Research*, *100*(B12), 24487–24498. https://doi.org/10.1029/95JB02630

Watts, A. B., Peirce, C., Collier, J., Dalwood, R., Canales, J. P., & Henstock, T. J. (1997). A seismic study of lithospheric flexure in the vicinity of Tenerife, Canary Islands. *Earth and Planetary Science Letters*, *146*(3–4), 431–447. https://doi.org/10.1016/S0012-821X(96)00249-X

Watts, A. B., & Ribe, N. M. (1984). On geoid heights and flexure of the lithosphere at seamounts. *Journal of Geophysical Research*, *89*(B13), 11152–11170. https://doi.org/10.1029/JB089iB13p11152

Watts, A. B., & ten Brink, U. S. (1989). Crustal structure, flexure, and subsidence history of the Hawaiian Islands. *Journal of Geophysical Research*, *94*(B8), 10473–10500. https://doi.org/10.1029/JB094iB08p10473

Watts, A. B., ten Brink, U. S., Buhl, P., & Brocher, T. M. (1985). A multichannel seismic study of lithospheric flexure across the Hawaiian-Emperor Seamount Chain. *Nature*, *315*(6015), 105–111. https://doi.org/10.1038/315105a0

Watts, A. B., Tozer, B., Harper, H., Boston, B., Shillington, D. J., & Dunn, R. (2020). Evaluation of shipboard and satellite-derived bathymetry and gravity data over seamounts in the northwest Pacific ocean. *Journal of Geophysical Research: Solid Earth*, *125*, e2020JB020396. https://doi.org/10.1029/2020JB020396

Watts, A. B., & Zhong, S. (2000). Observations of flexure and the rheology of oceanic lithosphere. *Geophysical Journal International*, *142*(3), 855–875. https://doi.org/10.1046/j.1365-246x.2000.00189.x

Watts, A. B., Zhong, S. J., & Hunter, J. (2013). The behavior of the lithosphere on seismic to geologic timescales. *Annual Review of Earth and Planetary Sciences*, *41*(1), 443–468. https://doi.org/10.1146/annurev-earth-042711-105457

Weigel, W., & Grevemeyer, I. (1999). The Great meteor seamount: Seismic structure of a submerged intraplate volcano. *Journal of Geodynamics*, *28*(1), 27–40. https://doi.org/10.1016/S0264-3707(98)00030-1

Wessel, P. (2016). Regional-residual separation of bathymetry and revised estimates of Hawaii plume flux. *Geophysical Journal International*, *204*(2), 932–947. https://doi.org/10.1093/gji/ggv472

Wessel, P., Luis, J. F., Uieda, L., Scharroo, R., Wobbe, F., Smith, W. H. F., & Tian, D. (2019). The generic Mapping Tools version 6. *Geochemistry, Geophysics, Geosystems*, *20*, 5556–5564. https://doi.org/10.1029/2019GC008515

White, R. S. (1993). Melt production rates in mantle plumes. *Philosophical Transactions of the Royal Society of London*, *342*(1663), 137–153. https://doi.org/10.1098/rsta.1993.0010

White, R. S., McKenzie, D., & O'Nions, R. K. (1992). Oceanic crustal thickness from seismic measurements and rare Earth element inversions. *Journal of Geophysical Research*, *97*(B13), 19683. https://doi.org/10.1029/92JB01749

Wilson, J. T. (1963). Continental drift. *Scientific American*, *208*(4), 86–103. https://doi.org/10.1038/scientificamerican0463-86

Wolfe, C. J., McNutt, M. K., & Detrick, R. S. (1994). The Marquesas archipelagic apron: Seismic stratigraphy and implications for volcano growth, mass wasting, and crustal underplating. *Journal of Geophysical Research*, *99*(B7), 13591–13608. https://doi.org/10.1029/94JB00686

Woods, M. T., & Davies, G. F. (1982). Late Cretaceous genesis of the Kula plate. *Earth and Planetary Science Letters*, *58*(2), 161–166. https://doi.org/10.1016/0012-821X(82)90191-1

Wright, N. M., Seton, M., Williams, S. E., & Müller, R. D. (2016). The Late Cretaceous to recent tectonic history of the Pacific Ocean basin. *Earth-Science Reviews*, *154*, 138–173. https://doi.org/10.1016/j.earscirev.2015.11.015

Zelt, C. A., & Forsyth, D. A. (1994). Modeling wide-angle seismic data for crustal structure: Southeastern Grenville Province. *Journal of Geophysical Research*, *99*(B6), 11687–11704. https://doi.org/10.1029/93JB02764

Zhong, S., & Watts, A. B. (2013). Lithospheric deformation induced by loading of the Hawaiian Islands and its implications for mantle rheology. *Journal of Geophysical Research: Solid Earth*, *118*, 6025–6048. https://doi.org/10.1002/2013JB010408

Zucca, J. J., Hill, D. P., & Kovach, R. L. (1982). Crustal structure of Mauna Loa Volcano, Hawaii, from seismic refraction and gravity data. *Bulletin of the Seismological Society of America*, *72*(5), 1535–1550. https://doi.org/10.1785/BSSA0720051535